ION DYNAMICS AND THE DYNAMO IN THE EDGE OF THE REVERSED-FIELD PINCH

by

Paul W. Fontana

A dissertation submitted in partial fulfillment of the

requirements for the degree of

Doctor of Philosophy

(Physics)

at the

University of Wisconsin–Madison

1999

ION DYNAMICS AND THE DYNAMO IN THE EDGE OF THE REVERSED-FIELD PINCH

Paul W. Fontana

Under the supervision of Professor Stewart C. Prager and Dr. Gennady Fiksel

At the University of Wisconsin–Madison

ABSTRACT

The magnetohydrodynamic (MHD) dynamo, $\langle \tilde{\boldsymbol{v}} \times \tilde{\boldsymbol{b}} \rangle$, and edge plasma flow profiles have been measured spectroscopically in the edge of the Madison Symmetric Torus (MST) Reversed-Field Pinch (RFP). The dynamo has been anticipated by theory and experiment to drive current not accounted for by applied or induced electric fields in the RFP. Previous spectroscopic measurements in MST have verified the presence of the dynamo in the core, and Langmuir probe measurements in the extreme edge have measured a dynamo produced from $\mathbf{E} \times \mathbf{B}$ velocity fluctuations. The present work employs a novel insertable optical probe, the Ion Dynamics Spectrometry Probe (IDSP), which has good spatial resolution and can access the edge ($0.75 < r/a < 0.95$), to extend the core spectroscopic velocity measurements into that region so as to measure the local dynamo during discrete flux-generation events ("dynamo events"). As a secondary result, equilibrium plasma flows in that region are also measured.

The velocity fluctuation measurements yield three substantial results. First, the dynamo balances Ohm's law in the region outside the reversal surface, accounting for the total current drive away from a dynamo event when the electric field is small, and balancing the electric field during the rise of the

dynamo event while the current responds modestly and more slowly. Second, the dynamo fluctuations in this region are found to consist mainly of modes with poloidal number m=0 and toroidal numbers n=1 and 2, corresponding to locally resonant magnetic modes. Third, the phase of the velocity fluctuations has been measured across their resonant surface and reflects the parity predicted by linear tearing mode theory.

The equilibrium toroidal flow profile shows flattening concurrent with the dynamo event, decelerating in a way previously seen in core flows and mode rotation. The deceleration is found to propagate outward from the core. The parallel momentum profile also flattens during the dynamo event. The radial velocity is measured to be significant and inward throughout a discharge, and to change by up to 3 km/s on average during a dynamo event; an explanation of this awaits further work.

Acknowledgements

As one of our number has said, "Science is not done in a vacuum." This is nowhere more true than on MST! A great many people have contributed to this dissertation and to my formation as a physicist, and they cannot all be recalled here. Still, some of the most significant contributions must not go without mention.

First and foremost, my thanks go to my advisor, Professor Stewart Prager. He provided me with an excellent combination of freedom and intellectual support, not to mention money. It has been a privilege to work with and for such a brilliant communicator and keen mind.

Dr. Gennady Fiksel's mind is simply the most scientifically fertile I have encountered. I owe him a great debt; in addition to providing me with the benefit of his close collaboration, he designed the IDSP and then graciously offered to let me reap its first physics fruits. And he's a nice guy, too.

I thank my defense committee for donating their time and input to help me wrap up my graduate student career in time to start my next job. They include Professor Paul Terry and Assistant Professor Cary Forest as readers and Professors Clint Sprott and Ray Fonck as nonreaders.

Thanks go also to Dr. Dan Den Hartog, who built the spectrometer, Dr. Abdul Almagri, who built the magnetic probe, Dr. Darren Craig, who built the Rogowski probe, Ching-Shih Chiang, who built the Langmuir probe, and Dr. Jim Chapman, who wrote much of the IDL code used in analyzing my data and much more that I pirated and modified for my own designs.

It has been my privilege to be involved intellectually, socially, and emotionally with a number of others who have participated in creating a stimulating and enjoyable environment. The know who they are: that crazy Espaniard, who is supposed to have had the coffee shop on its feet for me to come work in by now, the guy I took to IHOP to learn the difference between a pizza and a pancake, that biker dude, whom I leave as the Lone Inertial Ranger from the Sterling Hall days, the guy who commits random acts of desk violence and shouldn't get too comfortable just because I'm graduating, my partner from B_t transformer construction to hauling firewood to metaphysical contemplation, my Zen master who did the impossible for MST and is doing it now for MDX, the guy who made us realize we didn't actually play very many computer games, the one who's finishing soon and will be dangerous if he can ever figure out the difference between his Chardonnay glass and his Cabernet glass, the woman who knows "a whole lotta man" when she sees it, the poker night source term who knows a lot about a lot if you put a pile of wings in front of him, both the computer guys, the Energizer Bunny, the Magic 8-Ball, the whole bunch of

hibpies, the one working on her investment banking career, and all the other current and former grad students, scientists, and staff who have contributed to making grad school interesting. One last word to you all: Get to work!

Thanks to my local support network, in particular to Pam Bradford, Ruth and Troy Jacobson, and B.J. Infante, who supported me through the final stretch in the best way possible: with food.

Thanks to my father Paul and my mother Margaret, who have always provided love, care, and encouragement to pursue my quirky interests whether they understood them or not. I regret that Mum did not make it to see me reach this goal, but I know she has been helping me even in the last few months. Thanks to all my brothers and sisters, too, for their concern and encouragement; I can't imagine a family I would rather be a part of.

Finally, I would like to thank the American taxpayers who have enabled fusion and plasma research in this country to survive, since I and this work have been funded by a grant from the U.S. D.O.E.

"The smashing victory of the theoretical approach [to plasma physics] over the experimental approach lasted as long as a confrontation with reality could be avoided." - Hannes Alfvén

"How manifold are your works, O LORD! – In wisdom You have wrought them all." - Ps. 104:24

"Blessed be you, mighty Matter, irresistible Progression, Reality ever new-born; you who, by constantly shattering our mental categories, force us to go ever further in our pursuit of Truth.

"Blessed be you, universal Matter, limitless Time, unbounded Space, triple abyss of stars and atoms and generations; you who, by overflowing and dissolving our narrow standards of measurement, reveal to us the dimensions of GOD."
- Pierre Teilhard de Chardin, S.J.

This Work is Dedicated to the Memory of

Margaret Dorothy Fontana
1 March 1928 – 8 March 1999

Robert Joseph Fontana
29 July 1957 – 6 July 1999

Elizabeth Gail Fontana
6 June 1985 – 13 September 1994

Requiem æternam dona eis, Domine,
Et lux perpetua luceat eis.

Table of Contents

List of Figures

1: *Introduction*

1.1 The Need for the Dynamo in the Reversed-Field Pinch

By this point in history, the popular culture is aware of and has largely assimilated the radical ideas of the "modern" physics of quantum mechanics and relativity theory which threatened to render classical physics obsolete early in this century. Yet there is another slower, more recent revolution underway in the study of physics which the general public is only just beginning to grasp. It involves efforts to understand systems in the classical regime but of sufficient complexity as to render their solution intractable under classical techniques. A hallmark of these complex systems which the "neo-classical" theory attempts to capture is large-scale self-organization; that is, large-scale simple structure is seen to emerge from small-scale complex turbulent activity.[1] A preeminent example of this is the self-generation of large-scale magnetic fields in conducting fluids, an effect known as "the dynamo." One of the most ubiquitous manifestations of self-organization in nature, the dynamo occurs on scales ranging from stars and perhaps galaxies to planets to laboratory plasmas.[2]

The dynamo was first proposed to explain the existence of the Earth's magnetic field and sunspots in the 1930's. At that time T.G. Cowling demonstrated[3] that an azimuthally symmetric magnetic field cannot be maintained in steady state by fluid motion alone. As the argument applies equally well to toroidal laboratory plasma, it is summarized here as follows: Consider a steady toroidal magnetic topology of closed flux surfaces with toroidal axisymmetry. There exists at least one toroidal magnetic axis, on which $\mathbf{B} = 0$ but $\nabla\times\mathbf{B}$ is nonzero and has a toroidal component. Hence $\mathbf{j} = \nabla\times\mathbf{B}/\mu_0$ also has a toroidal component on axis by Ampère's law. In Ohm's law for a magnetofluid,[4] $\mathbf{E} + \mathbf{v}\times\mathbf{B} = \eta\mathbf{j}$, $\mathbf{v}\times\mathbf{B} = 0$ because $\mathbf{B} = 0$ there, leaving $\mathbf{E}$ with a toroidally symmetric toroidal component. Integrating this around the magnetic axis then gives a nonzero time derivative of poloidal flux from Faraday's law, $\oint \mathbf{E}\cdot d\mathbf{s} = -\frac{\partial}{\partial t}\int \mathbf{B}\cdot d\mathbf{A}$, contradicting the assumption of steady state without external drive. The conclusion is that such a steady field requires toroidal asymmetry (i.e. fluctuations) at least on the magnetic axis.

A similar argument can be applied to the steady-state field of a Reversed-Field Pinch (RFP), a toroidal magnetic plasma confinement device with the principal defining characteristic that the toroidal field B_ϕ decreases monotonically from the axis to the edge, passing through 0 for some flux surface interior to the plasma referred to as the "reversal surface" (Figure 1.2).[5] In this configuration the field cannot be sustained without fluctuations regardless of the presence of an external drive.[6,7] By an argument similar to Cowling's theorem, the nonzero radial derivative of B_ϕ (together with toroidal symmetry) ensures a poloidal current j_θ everywhere, which, assuming poloidal symmetry, cannot be driven at the reversal surface by $\mathbf{v}\times\mathbf{B}$, which has no poloidal component there.

Hence there must be a poloidal electric field E_θ. Applying Faraday's law this time in the poloidal sense around a contour lying dynin the reversal surface finds that the toroidal flux decays. In the absence of external drive, then, the RFP magnetic configuration can only be maintained by non-MHD effects or by both toroidal and poloidal symmetry-breaking magnetic fluctuations $\tilde{\boldsymbol{b}}$, which drive the steady state current through the $\mathbf{v}\times\mathbf{B}$ term in Ohm's law by correlating appropriately with asymmetries $\tilde{\boldsymbol{v}}$ in the fluid flow. This is precisely the "dynamo" mentioned above: the self-generation (or regeneration) of large scale magnetic field from small-scale structure. In the litterature this particular

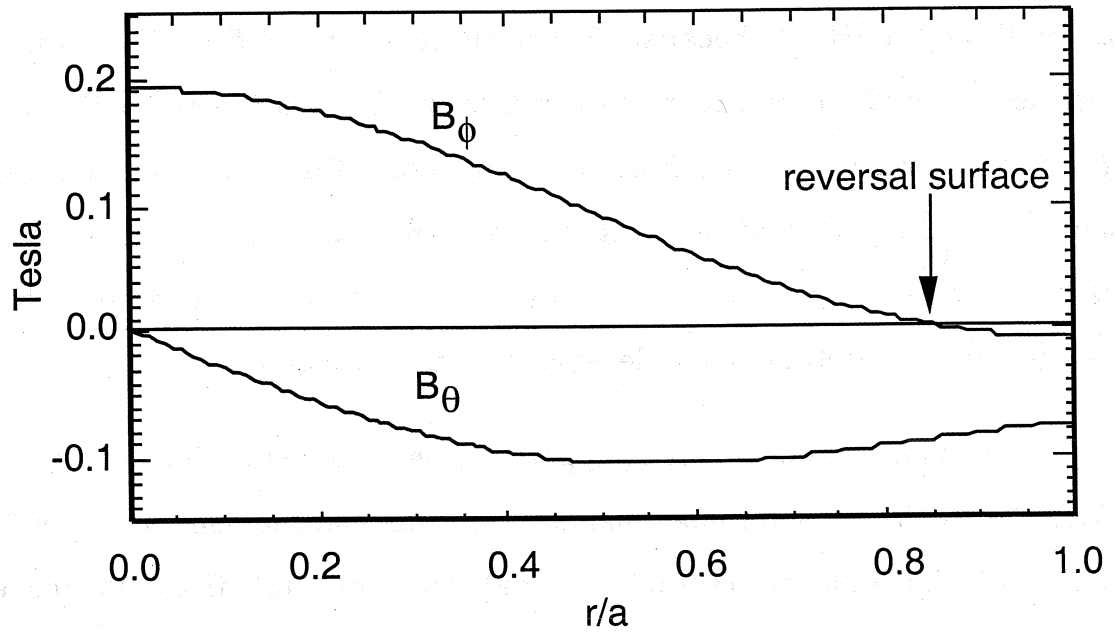

Figure 1.1. Typical RFP Magnetic Field Profiles. The toroidal field has a radial gradient everywhere except r/a = 0.0 and passes through zero near the edge.

manifestation of the dynamo is often referred to as the "α-effect", in reference to terminology employed in early geo- and astrophysical dynamo theory.[8] In that framework it is shown[9] that the mean-field average of the fluctuation-induced

e.m.f. is linear in the mean magnetic field and its derivatives, and that this term is able to sustain the field against resistive decay.

Experimental RFP's include external current drive, which could hypothetically act to sustain the magnetic field. However, Caramana and Baker[10] have modeled RFP discharges in the ZT-40 RFP without dynamo. Their model, a one-dimensional MHD simulation using the edge boundary conditions measurable in ZT-40 flat-topped and ramp-up discharges, showed that their applied drive is completely inadequate to explain the maintenance of their fields against resistive decay

All of this suggests the presence of dynamo in the steady state RFP. In addition, the toroidal flux in some RFP's is known to increase in discrete bursts, referred to herein as "sawtooth crashes" or "sawteeth" (Figure 1.2).[11,12] Current profile modeling has been used to determine the magnetic fields and the e.m.f. associated with these fast flux changes, resolved as a function of time. It is found that the parallel current profile (toroidal in the core, poloidal in the edge) flattens dramatically during these flux generation events, in a way which cannot be accounted for by the induced or applied e.m.f. The conclusion is that the supplemental e.m.f. – presumed to be the fluctuation-induced dynamo – is responsible for the flux generation. These sawteeth will synonymously be called "dynamo events" in this thesis.

In addition to the experimental modeling, extensive nonlinear simulations have been conducted, with similar results.[13,14,15,16] These simulations include magnetic and fluid fluctuations explicitly and allow direct study of $\langle \tilde{\boldsymbol{v}} \times \tilde{\boldsymbol{b}} \rangle$. The dynamo does in fact supply an appropriate e.m.f. in these simulations, and

furthermore the correlated fluctuations involved are identified in the code as resistive tearing instabilities, known to include most of the magnetic fluctuations in the RFP.

J. B. Taylor has developed a theory which captures a wide range of observed plasma dynamics by assuming that the plasma relaxes to a minimum energy state under the constraint of global conservation of magnetic helicity.[17,18] An understanding of the dynamo event from application of Taylor's relaxation theory to the RFP follows.[19,20] The RFP steady state, being driven, is close to but not entirely in a relaxed Taylor state. The current drive, consisting of a toroidal voltage, tends to drive more parallel current in the core than at the edge. This peaking of the parallel current profile is enhanced by resistive magnetic diffusion. Since in the preferred state the current profile is nearly flat, this drives the current away from relaxation, storing free energy as it does so in the radial parallel current gradient. When the current gradient becomes

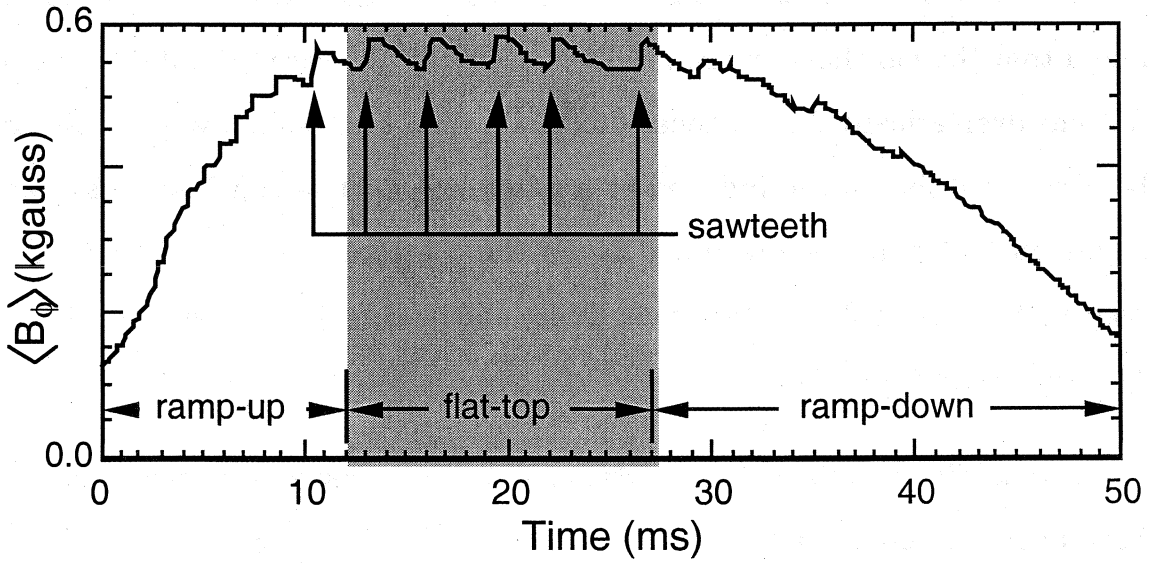

Figure 1.2. Flux Generation Events in the RFP. Shown is the average toroidal flux for a typical discharge, showing discrete bursts of dynamo activity.

large enough in regions where resistive tearing modes are resonant, they are destabilized, increasing in such a way as to provide current-flattening $\langle\tilde{v}\times\tilde{b}\rangle$. The plasma thus progresses back toward a relaxed state. Finally, As the current profile flattens the free energy source driving the instabilities goes away, and the tearing modes return to their quasi-stable inter-event level, reducing the dynamo as well.

1.2 Previous Dynamo Measurements in the RFP

Of course, all of the preceding discussion wants direct, experimental observation of the fluctuation induced dynamo $\langle\tilde{v}\times\tilde{b}\rangle$. Prior to the current work, there have been two sets of such measurements in the RFP. One has involved spectroscopic measurements of ion velocity fluctuations in the core (r/a < 0.6) of the Madison Symmetric Torus RFP (MST)[21], correlated with core-resonant magnetic fluctuations as measured with edge magnetic arrays.[22] The result was positive: the fluctuations produced an e.m.f. which within experimental uncertainties balanced Ohm's law. The experiment suffered somewhat from limitations imposed by the chord-averaged measurements provided by the diagnostics. However, the measurement found that although the m=1 magnetic modes are known to have broad eigenfunctions, the velocity fluctuations tend to correlate with a magnetic mode most strongly in the relatively narrow region of the mode's resonant surface; this suggests eigenfunctions for the velocity fluctuations which are more localized than those for magnetics.

The other RFP dynamo measurements had been made with insertable Langmuir probes in the extreme edge (r/a > 0.90) of several RFP's.[23,24,25] The probe measured velocity fluctuations only through inference from $\tilde{\mathbf{E}} \times \mathbf{B}$ and

$\nabla\tilde{\mathbf{P}} \times \mathbf{B}$ (diamagnetic) velocities. In the edge of the REPUTE-1 RFP the measured dynamo e.m.f. could not account for $\eta j_{\|}$–$E_{\|}$. This raises the question of whether velocity fluctuations other than those measured exist in this machine, or whether the missing e.m.f. is supplied by some other mechanism. In MST, however, while the diamagnetic fluctuations were found to be small, the dynamo calculated from the $\tilde{\mathbf{E}} \times \mathbf{B}$ velocity did balance Ohm's law. In the TPE-1RM20 RFP the situation was reversed from MST, with diamagnetic fluctuations dominating the dynamo, while still balancing Ohm's law.

1.3 Contribution of the Present Dynamo Measurement

The present work was done on MST, and is to be understood as complementary with the previous dynamo measurements there. The velocity fluctuations were measured using a novel insertable spectroscopic probe, the Ion Dynamics Spectrometry Probe (IDSP).[26] The probe has the advantages of localization and of access to the near edge of MST ($0.75 < r/a < 0.95$). Thus it extends the range and improves the localization of the previous spectroscopic measurements. Compared with the Langmuir probe measurements in MST, the present work provides the complete flow velocity fluctuation, not just $\tilde{\mathbf{E}} \times \mathbf{B}$ and diamagnetic; the result that at the extreme edge the measurements agree indicates that other contributions to the velocity fluctuations do not contribute to the dynamo there. In addition to the velocity measurements, local measurements of magnetic fluctuations, electric field, and current were also made to allow study of Ohm's law.

The work yields three substantial conclusions. First, in the region outside the reversal surface the measured dynamo balances Ohm's law. Away from the

dynamo event the parallel electric field is small; the dynamo is sufficient to drive the relatively small parallel current. During flux generation, the parallel electric field is large as expected; the dynamo simultaneously increases in the opposite direction to balance it, becoming large at the peak of the dynamo event, while the current rises more slowly and only modestly. Second, the dynamo fluctuations in this region are found to consist mainly of modes with poloidal number m=0 and toroidal numbers n=1 and 2. These correspond to the magnetic modes resonant at the reversal surface; i.e., the dynamo velocity fluctuations are related only to the locally resonant magnetic modes, and not to modes of large amplitude but which are resonant elsewhere. In addition, at the smallest radii (inside the reversal surface) there is some indication of the presence of high-n components in the spectrum, also corresponding to locally resonant tearing modes but here of poloidal mode number m=1. The implication is that the dynamo is produced not by the presence of the magnetic fluctuations *per se*, but only by the reconnection associated with these modes, which is localized to regions near their resonant surfaces. Third, since the velocity fluctuations in this region are all resonant at the same radius, we have taken advantage of the opportunity to measure their phase parity. They are found to display the parity predicted by linear MHD theory for tearing mode velocities, namely, $\tilde{v}_r$ undergoes a phase flip of π radians across the resonant surface while $\tilde{v}_t$ maintains constant phase. Under most conditions the presence at any given position of many modes with disparate resonant surfaces makes this measurement unfeasible; to our knowledge, ours constitutes the first direct observation of the tearing mode phase parity in the velocity.

1.4 Additional Measurements: Edge Equilibrium Flows

In addition to the study of the dynamo, this work includes as a secondary emphasis an empirical study of the equilibrium plasma flows (defined alternately as flux-surface averages or flows changing slowly with respect to fluctuations) in the RFP edge. The evolution of the toroidal velocity profile during a sawtooth is studied, including its rapid deceleration and re-acceleration. This phenomenon is seen to occur first in the core, followed later by the edge, with a delay as the effect propagates across the reversal surface. This is consistent with the theory that the deceleration is caused by torques applied to magnetic islands which are growing at the sawtooth.[27] Meanwhile, the equilibrium poloidal profile is found to change much less drastically at a sawtooth, although combining parallel velocity with local density measurements from a Langmuir probe to give parallel momentum shows significant flattening of the momentum profile with the sawtooth. This in interesting in the light of theories which predict similar behavior for parallel momentum transport.[28] There is a shear in v_p across the reversal surface, becoming stronger during the 0.5 ms following the crash due to acceleration of the core-side ions. A nonzero inward radial velocity is also measured, which remains to be explained.

The velocity profile has been measured during electrostatic current injection[29,30] to investigate flow shear as a cause of the improved confinement in that mode of operation; the result is that in the range observed the flow changes direction but the shear does not change significantly. Attempts to study the profile during good confinement produced with auxiliary poloidal current drive (PPCD)[31] were less successful due to degradation of the good confinement due to the presence of the IDSP at deep insertion, but a single-point measurement was

made showing the change in character of the toroidal flow as well as the reduction of dynamo in that regime.

REFERENCES

1 A. Hasegawa, Advances in Physics **34**, 1 (1985).

2 See, for example, articles by E.N. Parker (p. 141), F. Krause (p. 156), Hannes Alfvén (p. 179), and others, *Role of Magnetic Fields in Physics and Astrophysics*, ed. by V. Canuto (The New York Academy of Sciences, New York, 1975).

3 T. G. Cowling, Mon. Not. Roy. Astron. Soc. **94**, 39 (Nov. 1933).

4 See Chapter 4 for a derivation.

5 H.A.B. Bodin and A.A. Newton, Nucl. Fusion **20**, 1255 (1980).

6 C.G. Gimblett, *Proc. of the Reversed Field Pinch Theory Workshop*, H.R. Lewis and R.A. Gerwin, eds., Los Alamos Natl. Lab. Report LA-8944-C (Los Alamos, NM, 1980), p. 254.

7 S. Ortolani and D.D. Schnack, *Magnetohydrodynamics of Plasma Relaxation* (World Scientific, Singapore, 1993), pp. 99-103.

8 F. Krause and H.K. Rädler, *Mean Field Electrodynamics and Dynamo Theory* (Pergamon Press, New York, 1980).

9 by taking the mean-field average of the curl of Ohm's law, giving what is known as the "diffusion equation".

10 E.J. Caramana and D.A. Baker, Nucl. Fusion **24**, 423 (1984).

11 R.G. Watt and R.A. Nebel, Phys. Fluids **26**, 1168 (1983).

12 S. Hokin *et al.*, Phys. Fluids B **3**, 2241 (1991).

13 Y.-L. Ho, Ph. D. thesis, University of Wisconsin – Madison, Madison, 1988.

14 A. Sykes and J.A. Wesson, *Proc. 8th European Conf. on Cont. Fusion and Plasma Physics* (Czechoslovak Academy of Sciences, Prague, 1977), p. 80.

15 E.J. Caramana, R.A. Nebel, and D.D. Schnack, Phys. Fluids **26**, 1305 (1983).

16 D.D. Schnack, E.J. Caramana, and R.A. Nebel, Phys. Fluids **28**, 321 (1985).

[17] J.B. Taylor, Phys. Rev. Lett. **33**, 1139 (1974).

[18] J.B. Taylor, Rev. Mod. Phys. **58**, 741 (1986).

[19] Ortolani and Schnack, p. 87.

[20] Y.-L. Ho and G.G. Craddock, Phys. Fluids B **3**, 721 (1991).

[21] R.N. Dexter *et al.*, Fusion Technol. **19**, 131 (1991).

[22] D.J. Den Hartog, J.T. Chapman, D. Craig, G. Fiksel, P.W. Fontana, S.C. Prager, and J.S. Sarff, Phys. Plasmas **6**, 1813 (1999).

[23] H. Ji *et al.*, Phys. Rev. Lett. **69**, 616 (1992).

[24] H. Ji, A.F. Almagri, S.C. Prager, and J.S. Sarff, Phys. Rev. Lett. **73**, 668 (1994).

[25] H. Ji *et al.*, Phys. Plasmas **3**, 1935 (1996).

[26] G. Fiksel, D.J. Den Hartog, and P.W. Fontana, Rev. Sci. Instrum. **69**, 2024 (1998).

[27] D.J. Den Hartog *et al.*, Phys. Plasmas **2**, 2281 (1995).

[28] C.C. Hegna, Phys. Plasmas **5**, 2257 (1998).

[29] D. Craig, Ph. D. thesis, University of Wisconsin–Madison, Madison (1998).

[30] D. Craig*et al.*, Phys. Rev. Lett. **79**, 1865 (1997).

[31] M.R. Stoneking, N.E. Lanier, S.C. Prager, J.S. Sarff, and D. Sinitsyn, Phys. Plasmas **4**, 1632 (1997).

2: *Diagnostic Tools and Techniques*

2.0 Introduction

In this chapter the principal diagnostics used for investigations of the ion dynamics in the edge of MST will be discussed. This includes discussions of the IDS and the IDS probe, the insertable magnetic pickup probe and Rogowski probe, and triple Langmuir probe. Special emphasis will be given to the techniques involved in measurements with the specialized passive spectrometry system. This will be followed by a discussion of analytical techniques including toroidal mode analysis, a technique called "pseudo-spectrum analysis" for inferring mode structure of a signal by comparison with edge magnetics, and sawtooth-ensembled correlation analysis, all of which will be used in the investigations of subsequent chapters. Readers who are interested in experimental results can skip most of this chapter with impunity, although they may want to skim the last two sections to become familiar with my usage of various mathematical terms for which conventions in definitions may vary.

2.1 The Ion Dynamics Spectrometer (IDS)

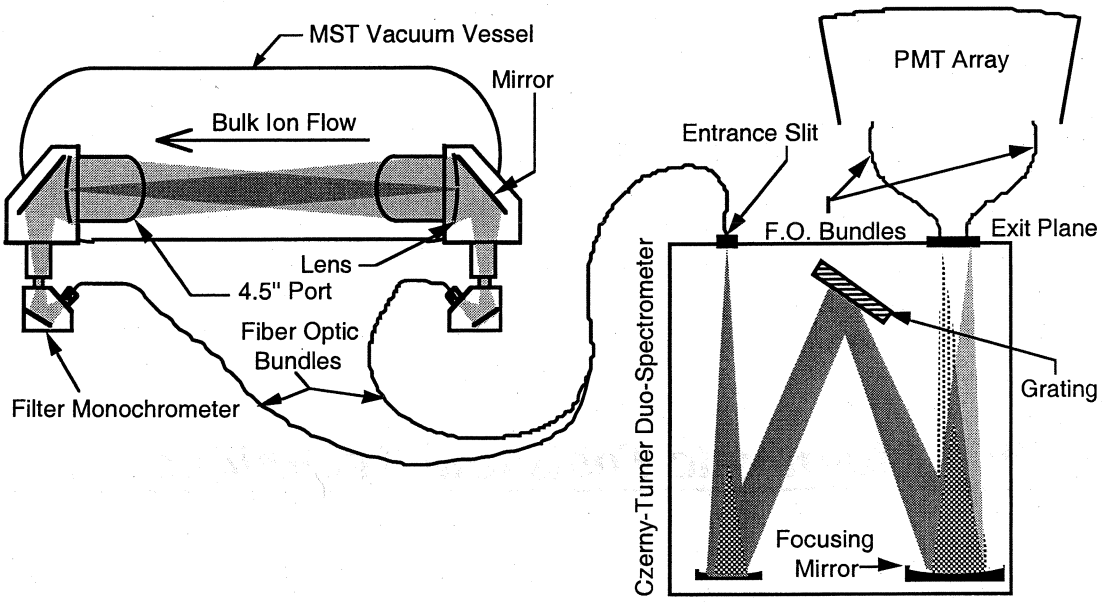

Figure 2.1. The Ion Dynamics Spectrometer (IDS), shown in its conventional configuration viewing the plasma through two opposed toroidal chords.

All of the new results of this work involve measurements made with a novel insertable optical probe designed to collect light to be used in Doppler spectroscopy from a localized region of the plasma. The probe itself is an attachment to a passive spectroscopy system known as the Ion Dynamics Spectrometer (IDS). The spectrometer is covered in detail elsewhere[1,2], but a presentation of some of its features relevant to the current work is in order.

The IDS is a *f*/10 1.0 m focal length Czerny-Turner style "duo"-spectrometer, able to process light collected in two fused-silica fiber optic bundles simultaneously. As designed, the spectrometer views the plasma through two antiparallel toroidal chords. In this configuration the two simultaneous views obviate the need for absolute calibration of the spectrometer. When used instead

with the IDS probe, they allow for simultaneous measurements of two components of the plasma velocity, as described in the next section.

The light collected by the two IDS views is incident on a 1180 groove/mm diffraction grating. The light exits the spectrometer in two sets of sixteen channels evenly spaced in wavelength. In nth order each view has a range of about 2.0/n nm and a resolution of about 0.125/n nm, values which are determined by the dispersion of the grating and the configuration of the channels exiting the spectrometer. This setup allows observation of isolated radiation emission lines from the plasma, which can then be analyzed for their Doppler shift and Doppler broadening to calculate the species' velocity and temperature. The spectrometer's design is optimized for measurements of the Cv 227.09 nm line made in fifth order with temperatures on the order of 10^2 eV, but has also been used effectively with other lines and impurities.

Each of the 32 channels of the spectrometer is amplified with a separate photomultiplier tube (PMT) operating in pulse mode and biased to about 500 V. The PMT output is amplified by high-gain I/V amplifiers, low-pass filtered, and finally digitized. The frequency response of the entire system is fairly flat to 250 kHz (down 5 dB from 5 to 250 kHz), and it is digitized at 1 MHz. Such fast time resolution is one of the primary features of the IDS system and is critical in the fluctuation analyses that follow.

In its conventional setup (Figure 2.1), the IDS is designed to collect light emanating from deep inside the plasma along long lines of sight. This penetrating power carries a twofold cost. First, like measurements from most passive plasma diagnostics, IDS measurements made in this way are inherently

nonlocal. The integration of light from all points along the instrument's lines of sight tends to wash out small scale fluctuations and confuses the interpretation of IDS observations. Second and related, the emissivity profiles of most plasma impurity species and the geometry of the various lines of sight of the IDS system render edge ion dynamics measurements difficult to impossible. Increasing awareness of the distinctive character of edge plasma dynamics and of the importance of their role in global issues such as energy confinement and particle transport makes it desirable to find a way to apply the power of the IDS system to the outermost regions of the plasma. The desire for localization and access to the plasma edge was the motivation for the construction of the IDS "probe" described in the next section.

2.2 The Ion Dynamics Spectrometry Probe (IDSP)

The IDSP overcomes the limitations of conventional IDS spectroscopy by collecting light only from a localized edge region of the plasma. The probe has a boron nitride housing which allows fused silica fibers to be inserted into the edge of the plasma, and it also supports boron nitride view dumps which limit the light collection area viewed by the fibers to a 5 cm x 5 cm region, thus achieving the spatial localization (Figure 2.2). Light collected by the fibers is then transmitted to the IDS system and the signals from the two views are analyzed, amplified, and stored in the conventional way. The frame supporting the view dumps is offset from the plane of view and has a large hole through the center to minimize any obstruction it might cause to the plasma flow it is intended to measure. The lines of sight are crossed at a right angle. This allows simultaneous measurements of two components of the ion velocity, which can be analyzed into the radial component and a perpendicular component selected by

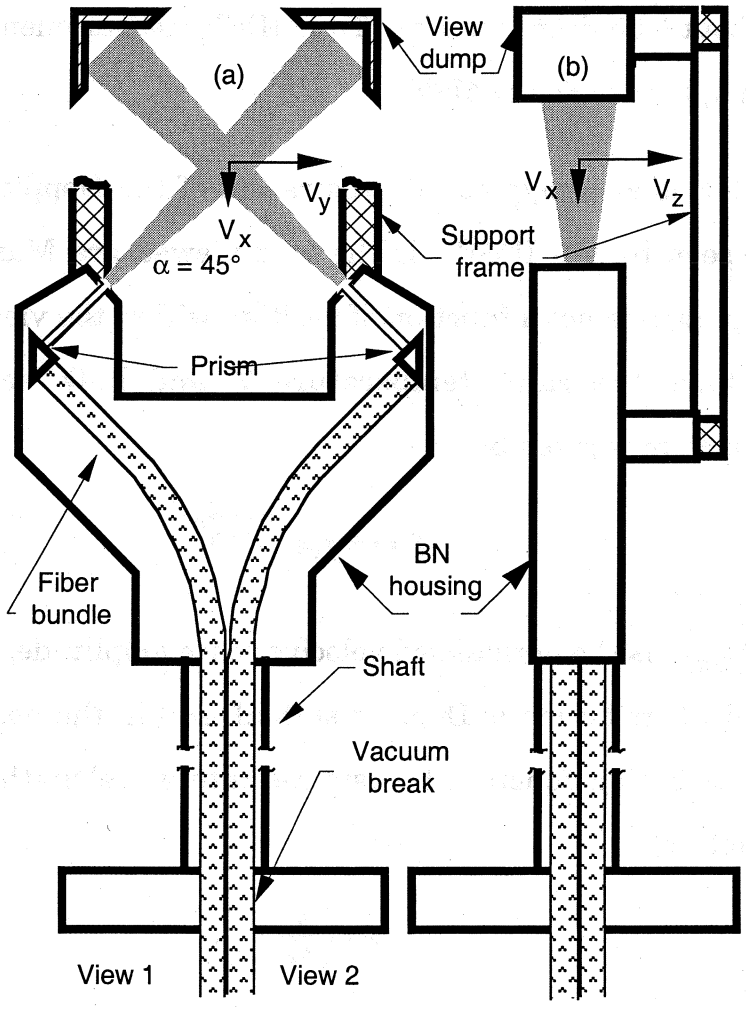

Figure 2.2. The Ion Dynamics Spectrometry Probe (IDSP). (a) Top view. (b) Side view.

rotating the probe about its radial axis. The perpendicular component is typically selected to be either toroidal or poloidal. The size of the probe restricts its use to one of the available $4^1/_2$ in. ports on MST, located toroidally at 138°T and 222°T and poloidally at 19°P. Measurements have been successfully made in to a depth of r/a=0.77, though at the very deepest insertions the light is often contaminated by broad-band pollution speculated to be black body radiation emanating from the overheating view dumps. (All radial measurements will be given with respect to the center of the viewing area of the IDSP; the front edge of

the probe is about 0.05 deeper in r/a). Thus IDSP measurements are essentially of the outer-midplane region of MST.

Figure 2.3 is an exaggerated illustration of the Doppler-broadened and -shifted light seen by the IDSP. If the ions viewed are Maxwellian and the distribution function is not a function of position within the viewing area (i.e. all ions viewed have the same temperature T and bulk velocity v_o), their distribution function is given by

$$f(v) = f_v e^{-\frac{m(v-v_o)^2}{2T}},$$

where $f_v = \sqrt{m/2\pi T}$ is the normalized velocity space amplitude. Light emitted by each ion in this distribution is Doppler shifted, and in the nonrelativistic limit $v << c$, the distribution function transforms into wavelength space using the change of variables

$$v = \left(\frac{\lambda}{\lambda_o} - 1\right)c,$$

$$v_o = \left(\frac{\Delta\lambda}{\lambda_o}\right)c$$

to give

$$f(\lambda) = f_\lambda e^{-\frac{mc^2}{2T}\frac{(\lambda-\lambda_o-\Delta\lambda)^2}{\lambda_o^2}},$$

where $f_\lambda = \frac{c}{\lambda_o} f_v$ is the normalized wavelength space amplitude, λ_0 is the wavelength of the unshifted line, and $\Delta\lambda$ is the Doppler shift of the centroid of the distribution from λ_0. This function is nearly proportional to the wavelength distribution seen by the spectrometer, subject to the assumptions stated above and to constraints imposed by the spectrometer's finite resolution. A velocity

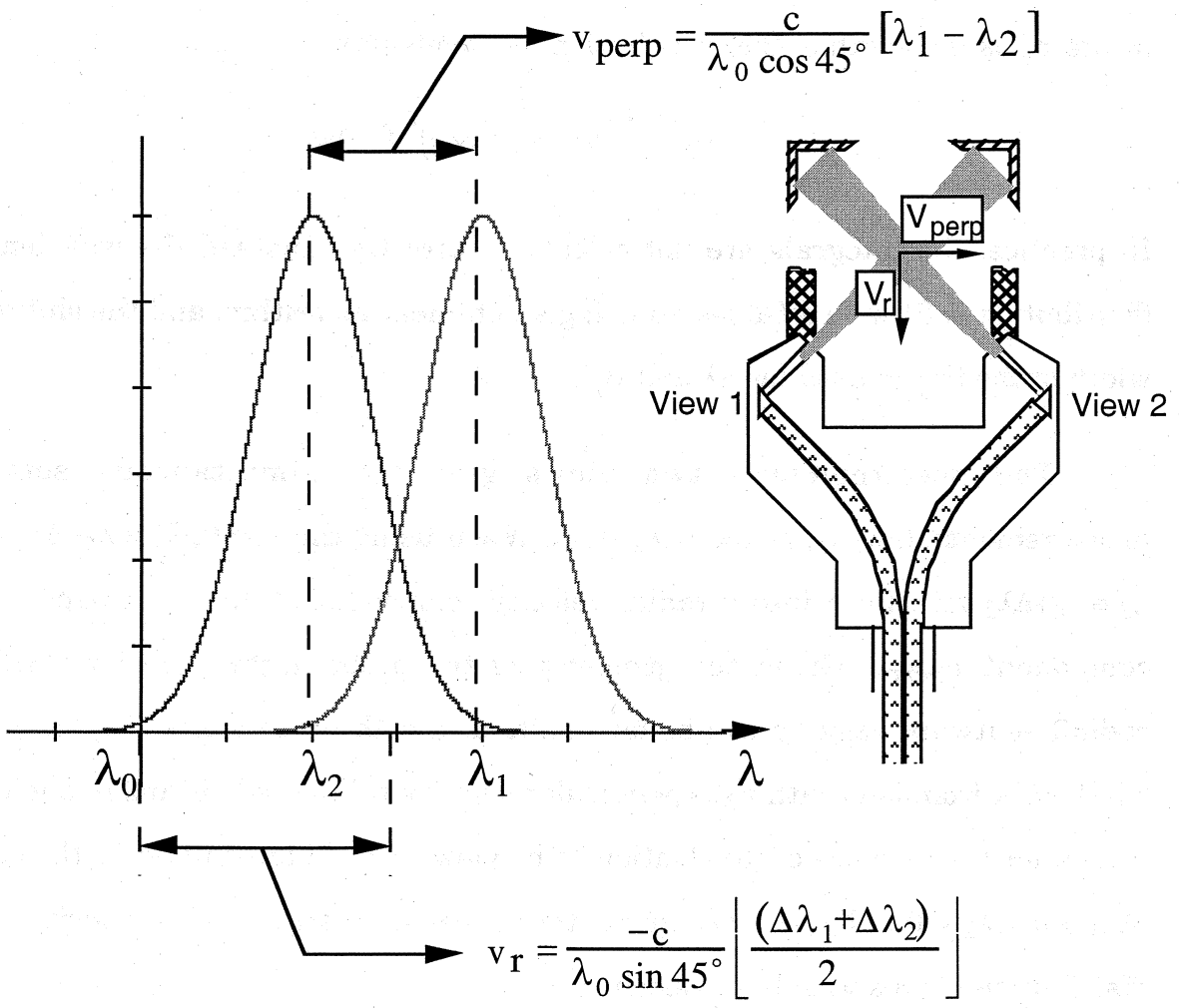

Figure 2.3. Spectroscopy with the IDSP. A cartoon of the Doppler-shifted line seen in each view of the probe.

and temperature of the emitting ion impurity species can therefore be extracted from moments of the measured distribution, calculating the velocity from the shift in wavelength of the centroid as given above with

$$\Delta\lambda = \int (\lambda - \lambda_o) f(\lambda) d\lambda,$$

and the temperature from the relationship

$$T = \frac{mc^2\sigma_\lambda^2}{\lambda_o^2},$$

where σ_λ is the width of the distribution in wavelength,

$$\sigma_\lambda^2 = \int \left(\lambda - \left(\lambda_o + \Delta\lambda\right)\right)^2 f(\lambda) d\lambda .$$

In practice, the integrals are not calculated directly. Instead the wavelength distribution is fit with a Gaussian using a nonlinear algorithm, and the shift and width of the fit are used for $\Delta\lambda$ and σ_λ.

The spectrometer's two views give two simultaneous sets of measurements, $(\Delta\lambda_1, \sigma_{\lambda 1})$ and $(\Delta\lambda_2, \sigma_{\lambda 2})$. When using the IDSP, $\lambda_1 \equiv \lambda_0 + \Delta\lambda_1$ and $\lambda_2 \equiv \lambda_0 + \Delta\lambda_2$ transform into a radial velocity component v_r and a perpendicular component v_{perp}. Given the geometry of the probe, light from ions with a radially-outward velocity will be blue-shifted in both probe views ($\Delta\lambda_1, \Delta\lambda_2 < 0$), while light from ions with a perpendicular velocity will be red-shifted in one view (taken for the purpose of illustration to be view 1) and blue-shifted in the other ($\Delta\lambda_1 > 0, \Delta\lambda_2 < 0$). To be more quantitative, consider an ion with velocity (or a distribution of ions with bulk velocity)

$$\boldsymbol{v} = v_{perp}\hat{\boldsymbol{p}} + v_r\hat{\boldsymbol{r}} ,$$

where $\hat{\boldsymbol{p}}$ and $\hat{\boldsymbol{r}}$ are unit vectors in the perpendicular and radial directions, respectively. Define unit vectors $\hat{\boldsymbol{v}}_1 = -\cos\alpha\hat{\boldsymbol{p}} + \sin\alpha\hat{\boldsymbol{r}}$ and $\hat{\boldsymbol{v}}_2 = \cos\alpha\hat{\boldsymbol{p}} + \sin\alpha\hat{\boldsymbol{r}}$ in the directions of the lines of sight, where $\alpha = 45°$ is the angle between the perpendicular direction and line-of-sight 1. Then the velocity v_1 and v_2 measured in each view is given by

$$v_1 = \boldsymbol{v} \bullet \hat{\boldsymbol{v}}_1 = -v_{perp}\cos\alpha + v_r \sin\alpha$$

$$v_2 = \boldsymbol{v} \bullet \hat{\boldsymbol{v}}_2 = v_{perp}\cos\alpha + v_r \sin\alpha .$$

Solving for v_r and v_{perp} and substituting for v_1 and v_2 in terms of the Doppler shift seen in each view gives

$$v_r = \left(-\frac{(\Delta\lambda_1 + \Delta\lambda_2)}{2} \right) \frac{c}{\lambda_o \sin\alpha}$$

$$v_{perp} = (\lambda_1 - \lambda_2) \frac{c}{\lambda_o \cos\alpha}.$$

The relative calibration of the spectrometer poses a special problem for v_r, which is proportional to the *average shift* in wavelength of the two views. Calculating an absolute value for v_r therefore requires knowledge of where the unshifted line λ_0 lies with respect to the output of the spectrometer; i.e., the spectrometer must be absolutely calibrated. This is a difficult measurement, and its details are discussed in the next chapter. Fortunately, many measurements require only the velocity fluctuation $\tilde{v}_r$, which is independent of any offset in the spectrometer, and not the equilibrium value of v_r. Furthermore, this caveat does not affect v_{perp} or $\tilde{v}_{perp}$, which depend only on the *difference between the shifts* in view 1 and view 2 and can consequently be calculated absolutely regardless of the spectrometer offset.

For all the IDSP measurements made in this thesis, the HeII 4685.7 Å line has been used. This line has several advantages. First, the mass and charge state of this species make it as close as an impurity species can get to the bulk hydrogen ions in the discharges studied. This forfends the perennial bugaboo of impurity spectroscopy concerning whether the measured dynamics actually reflect the bulk. Furthermore, since helium is not well-recycled by boron nitride the fear of observing only gas emitted by the probe is avoided. The plasma fuel is typically doped with helium both before and at the start of the discharge to

increase the signal; before data were taken tests were done to determine levels of doping which would not affect the plasma conditions strongly. The momentum relaxation rate between two ion species is given approximately by[3]

$$\upsilon_s \approx 6.8\text{x}10^{-8}\,\text{cm}^3/\text{s}\cdot n_{i'} Z^2 Z'^2 \ln\Lambda \frac{\mu'^{1/2}}{\mu}\left(1+\frac{\mu'}{\mu}\right)T^{-3/2},$$

where primes denote the background, $n_{i'}$ is the background ion density, μ and μ' are the masses in a.m.u., $\ln\Lambda$ is the Coulomb logarithm, and T is the temperature of the background ions. For HeII in the edge hydrogen plasmas of MST, this comes out to the order of 10^4/s, so doping gas which has been introduced early in the discharge will have acclimated to the background plasma by the time the IDSP measurements are made. There is some concern about the impurity velocity fluctuations reflecting those of the bulk, since IDSP measurements are typically made at 100 kHz or faster; however, the relevant dynamics in the present results take place at less than 10 kHz, slowly enough to allow the velocities to match. The helium emission profile has been found to be flat throughout the edge region of the plasmas studied here. The line used is also relatively isolated, although some problems with small unidentified lines close enough in wavelength to be seen simultaneously by the spectrometer do occasionally have to be dealt with.

The HeII 4685.7 Å line is viewed by the IDS in second order. This determines the sensitivity of the spectrometer; in second order the sixteen channels evenly span about 10 Å. For this line, a velocity v and temperature T appear to the spectrometer as

$$\Delta\lambda = 1.56\text{x}10^{-2}\,\text{Å}\frac{v}{1\,\text{km/s}}$$

$$= 2.50\text{x}10^{-2}\,\text{channels}\frac{v}{1\,\text{km/s}}$$

$$\sigma_\lambda = 0.153\text{Å}\sqrt{T/1\text{eV}}$$

$$= 0.245\text{channels}\sqrt{T/1\text{eV}} \quad \text{(full width).}$$

At the low edge ion temperatures of MST, the Doppler broadening is significantly less than a spectrometer channel, unfortunately rendering IDSP temperature measurements impossible under most conditions. Temperature measurements with this line are also complicated by its finite fine structure, on the order of an Angstrom, which in future measurements with a more sensitive spectrometer will need to be subtracted from the line width before calculating the temperature. The Doppler shift, though even smaller than the broadening as compared with the channel width, is nonetheless measurable with a precision on the order of 1 km/s. This sensitivity has two sources: first, overlapping transmission functions of the detectors ensure signal in at least three channels for even very narrow lines, and second, the centroid of the distribution is easier to fit than the temperature, requiring only enough information about the distribution to fit the first moment rather than the second.

2.3 Other Diagnostic Probes

2.3.1 The Insertable Magnetic Probe

In addition to local velocity measurements, local magnetic measurements are critical to this work. They provide three sets of information. First, they are used to measure the local safety factor profile, q(r), in the edge of MST, and in particular to identify the position and motion of the reversal surface, where modes of poloidal number m=0 are resonant. Second, $\dot{b}_t(r)$ is used in the

calculation of poloidal electric field near the wall. Third and most significantly, $\tilde{b}_r$ and $\tilde{b}_t$ are correlated with velocity fluctuations to measure the MHD dynamo. For all of these measurements an insertable probe consisting of a collection of magnetic pickup coils was used (Figure 2.4).[4] The coils are wound around the boron nitride coil form shown in the figure. The deepest coil form bears three pickup coils: a one-turn Bp coil with rectangular dimensions of 3.0 cm radially and approximately 0.4 cm toroidally (calibrated A_{eff}=0.90 cm^2), a two-turn B_t coil with rectangular dimensions of 3.0 cm radially and approximately 0.21 cm poloidally (A_{eff}=2.40 cm^2), and an 80-turn B_r coil with cylindrical dimensions of approximately 0.16 cm radius and a 0.97 cm radial extent (A_{eff}=7.74 cm^2). The coils are electrostatically shielded with silver paint and clad in a sheath of boron nitride to shield them from the plasma. Their signals are typically analog-integrated and digitized at 200 kHz.

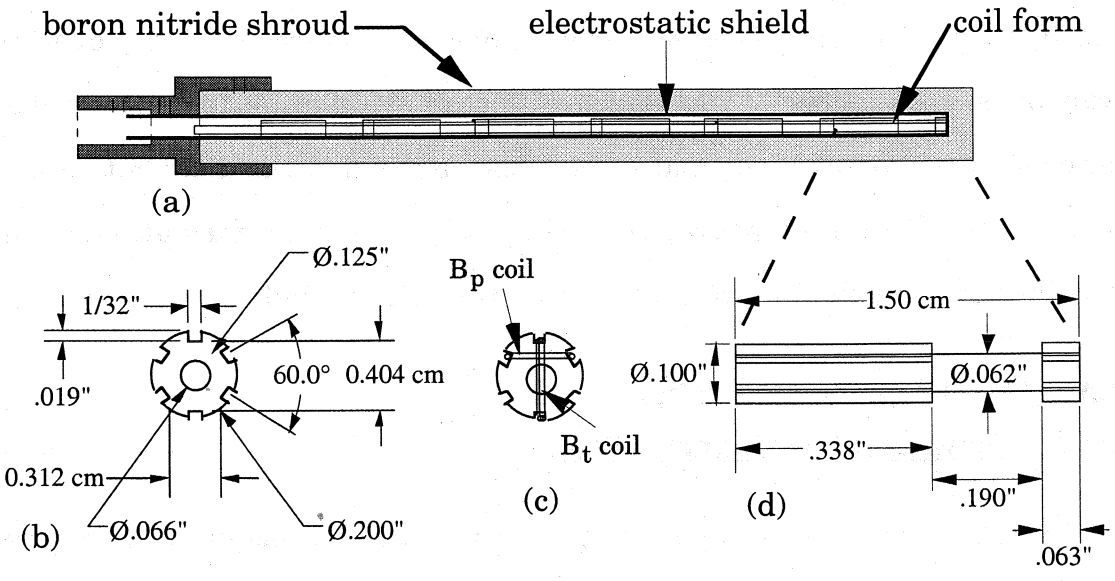

Figure 2.4. The Insertable Magnetic Probe. Shown are (a) the probe shaft, showing the relative orientation of multiple coil forms, (b) a single coil form end view, with dimensions, (c) the coil form with poloidal and toroidal windings, end view, and (d) the coil form, side view, with dimensions, showing the orientation of the radial coil.

2.3.2 The Rogowski Probe

The edge parallel current profile measurements in this thesis were made using an insertable Rogowski coil[5,6]. The probe carrying the Rogowski coil also has three single-turn magnetic coils, a circular coil used for B_p and two saddle-shaped coils for B_t and B_r. The probe head is encased in a boron nitride ring which has an inner diameter of 1.82 cm; the current density is obtained by dividing the total current measured by the area of this hole. The magnetic field coils, in addition to their use both in aligning the probe and correcting for imperfections in the Rogowski coil winding, provide an additional triplet of magnetic field measurements. These signals have been used for some dynamo measurements in lieu of the magnetic probe to corroborate the results of Chapter 4.

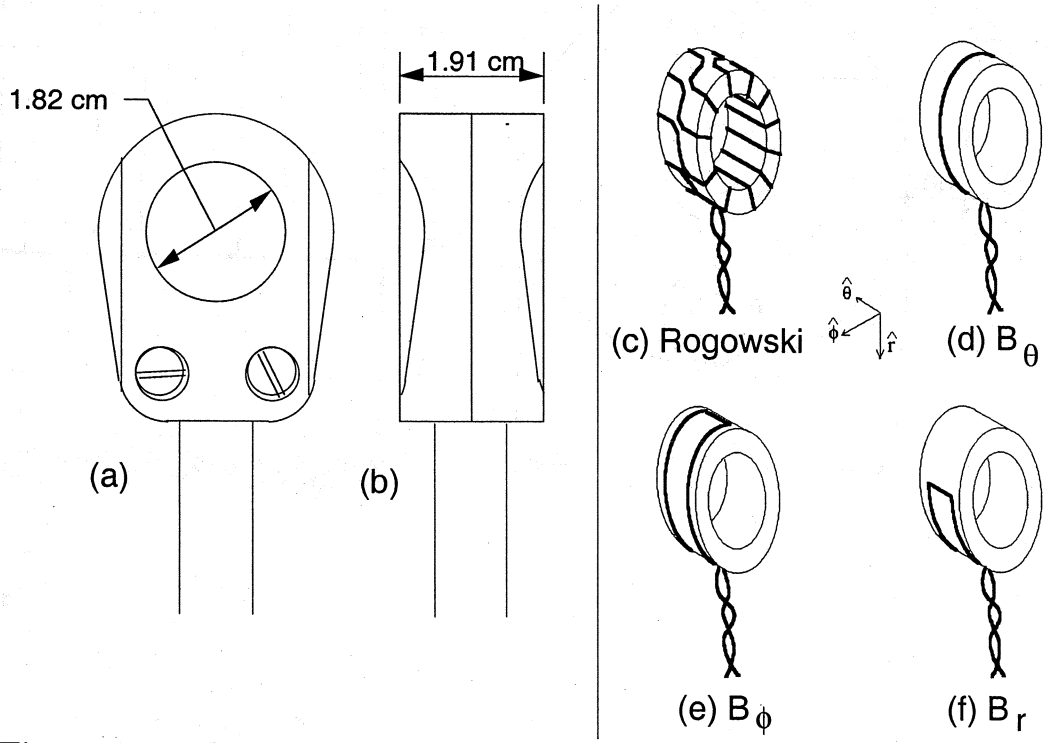

Figure 2.5. The Rogowski Probe. Left: the boron nitride housing, (a) in top view, showing the 1.82 cm-diameter current collection hole, and (b) in side view. Right: the coil form, showing (c) a few representative turns of the Rogowski coil, (d) the circular poloidal (parallel) magnetic field coil, (e) the toroidal field saddle coil, and (f) the radial field saddle coil.

2.3.3 The Triple Langmuir Probe

Equilibrium and fluctuating electron density measurements in this thesis were made using an insertable three-tip Langmuir probe[7]. A large bias V_{31} is maintained between tips 1 and 3 while they float with respect to ground, so as to collect a current I in tip 3, which is measured with a low-impedance voltage divider (Figure 2.6). Meanwhile tip 2 is allowed to float at the plasma potential, and the potential V_{21} between tips 1 and 2 is measured. It can be shown[8] that under the conditions of the edge plasmas in MST, the electron density n is given

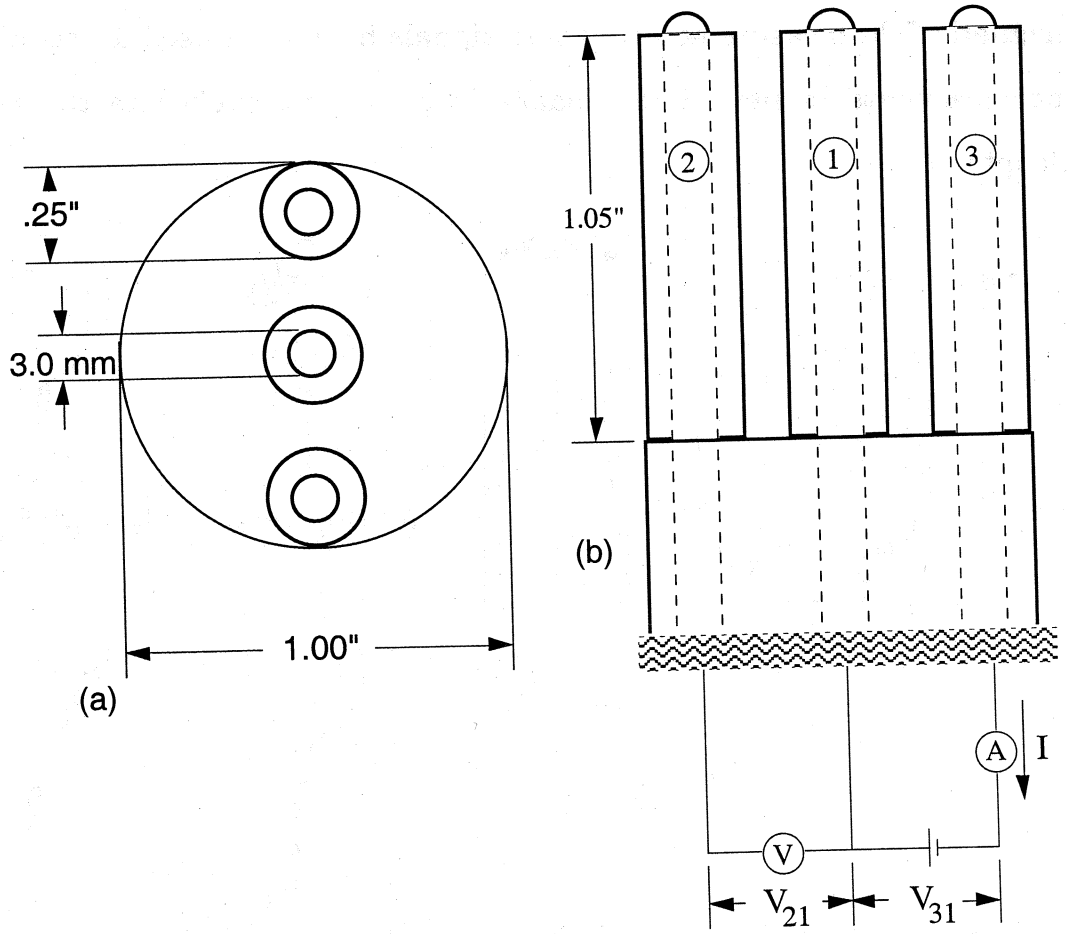

Figure 2.6. The Triple Langmuir Probe. (a) End view. (b) Side view and cartoon schematic showing bias applied between tips 1 and 3, measured current collected in tip 3, and potential measured between tips 1 and 2.

by

$$n = \frac{\exp(1/2)}{AeC_s} I_+,$$

where A is the ion collection area of probe tip 1, C_s is the ion sound speed ($C_s \approx \sqrt{T_e / m_i}$ for these plasma conditions), and I_+ is the ion saturation current. It can be shown that if the probe bias $V_{31} >> T_e/e$, then I_+ and T_e relate to the measured current I and potential V_{21} through

$$T_e = \ln\left(1 + \frac{A_3}{A}\right) eV_{21}, \text{ and}$$

$$I_+ = \frac{I_1}{\exp(eV_{21}/T_e) - 1}.$$

Here A_3/A is a correction factor on the order of 10^{-1} to account for differences in ion collection area between tip 3 and tip 1. Note that the T_e dependence of I_+ cancels, so that n depends on T_e only as $T_e^{-1/2}$; uncertainties and systematic errors in the electron temperature do not affect it strongly.

2.4 Correlation Ensemble Analysis

Statistical analysis techniques have been employed extensively throughout this work. This section gives relevant mathematical definitions as they are used in the rest of the thesis and highlights some of the details of these techniques.

First, for the sake of consistency of terminology a review of fluctuation analysis is in order. Consider a quantity X to be measured in the plasma as a function of time. To the extent that good closed flux surfaces exist in the plasma,

X has a theoretically well-defined average over that flux surface $\langle X \rangle$, which can be represented symbolically by

$$\langle X \rangle = \frac{\oint X \, dA}{\oint dA},$$

where the notation $\oint \ldots dA$ represents integration over the flux surface. The quantity X can then be separated into this average part plus a fluctuation $\tilde{X}$ defined by $\tilde{X} = X - \langle X \rangle$, which by definition averages to 0 over the flux surface.

In practice, even if the location of a flux surface were known precisely, measuring this average would require an extensive two-dimensional array of similar diagnostics distributed toroidally and poloidally about the machine. Since this is unfeasible with even our most complete diagnostics systems, some assumptions must be made to arrive at an approximation to the average. For example, if the plasma is rotating with respect to the laboratory frame of reference in the appropriate way and poloidal asymmetry is small, a measurement made at a single toroidal and poloidal location over time will eventually sample points from an entire flux surface. In this case the flux surface average of X is approximated by a simple time average. This scheme assumes, however, that the plasma conditions are not changing over the averaged time window, and in particular that the flux surfaces are not moving radially during this time. It is therefore inadequate for analysis of dynamical changes in the plasma, as happen, for example, during the dynamo events ("sawteeth") in MST. Under such circumstances it becomes necessary to collect an ensemble of time windows during each of which the plasma undergoes a similar dynamic change, and to perform the average not over time but across the realizations in this ensemble. If the orientation in the laboratory frame of the

flux surfaces does not depend strongly on time relative to this dynamic event then this "event ensemble" again provides an approximation to a flux surface average. Furthermore, even if the flux surfaces are moving radially during the event, so long as their motion is similar from one realization to another such an ensemble will at any given point in time relative to the event be sampling approximately the same surface. These event ensembles therefore accomplish with a single-point measurement an approximate flux-surface average which preserves the time dependence of the quantity under observation.

In addition to single quantities, this event ensembling technique can be applied to products of two or more quantities. Although as noted above fluctuations of a single quantity average to zero by definition over a flux surface, combinations of even small fluctuations can contribute mean-field effects. For example, if in addition to measuring X one also measures Y, the flux-surface-averaged value of XY is given by

$$\langle XY\rangle = \langle X\rangle\langle Y\rangle + \left\langle \tilde{X}\right\rangle\langle Y\rangle + \langle X\rangle\left\langle \tilde{Y}\right\rangle + \left\langle \tilde{X}\tilde{Y}\right\rangle$$

$$= \langle X\rangle\langle Y\rangle + \left\langle \tilde{X}\tilde{Y}\right\rangle,$$

i.e. $\langle\tilde{X}\tilde{Y}\rangle$ may survive the flux-surface average although terms linear in fluctuations do not. Close inspection of terms such as this reveals a great deal about fluctuation-induced processes in the plasma, including transport and the dynamo.

The value of the quantity $\langle\tilde{X}\tilde{Y}\rangle$ is determined by four (time dependent) factors: the amplitudes of $\tilde{X}$ and $\tilde{Y}$, the (phase-independent) correlation between $\tilde{X}$ and $\tilde{Y}$ (a factor between 0 and 1), and their relative phase (a factor from -1 to

1). The literature is not consistent about the terminology or definitions of these factors, but the conventions used in this work follow.

To determine the correlation and phase we will need the Hilbert transform $X^{\dagger}$, defined as

$$X^{\dagger}(t) \equiv \iint X(t')e^{i\left(2\pi ft+\frac{|f|}{f}\frac{\pi}{2}\right)}e^{-i2\pi ft'}\,dt'\,df\ .$$

In other words, $X^{\dagger}$ is X with each Fourier component phase-shifted by $\pi/2$. Using this to calculate the factors in the correlation allows us to define

$$\langle\tilde{X}\tilde{Y}\rangle = |\tilde{X}|\,|\tilde{Y}|\gamma\cos\delta, \qquad \text{where}$$

$$|\tilde{X}| = \langle\tilde{X}^2\rangle^{1/2},$$

$$\gamma = \frac{\left(\left\langle\tilde{X}\tilde{Y}\right\rangle^2 + \left\langle\tilde{X}\tilde{Y}^{\dagger}\right\rangle^2\right)^{1/2}}{|\tilde{X}||\tilde{Y}|}, \quad \text{and}$$

$$\delta = \tan^{-1}\left(\frac{\left\langle\tilde{X}\tilde{Y}^{\dagger}\right\rangle}{\left\langle\tilde{X}\tilde{Y}\right\rangle}\right).$$

Here γ will be referred to as the "correlation" of X and Y and will sometimes be denoted corr(X,Y), and δ (or $\cos\delta$ where the meaning is unambiguous) will be referred to as the "phase" and will equivalently be denoted phase(X,Y). This usage differs from that of some references, which use the term "correlation" for the entire factor of $\gamma\cos\delta$. This definition does not distinguish the low correlated product of fluctuations of different frequencies from that of fluctuations of the same frequency but different phase. The advantage of the definition above is that these effects are separated out; signals which differ *only*

by a phase shift (for example, $\cos(\omega t)$ and $\sin(\omega t)$) will still have high γ, even though the correlated product may be low.

The time-dependent correlation and phase have frequency-domain analogs referred to herein as the "coherence" ($\gamma(f)$, coh(X,Y)) and the "coherence phase" ($\delta(f)$, coh_phase(X,Y)) of the signals. By giving frequency-dependent information at the expense of time-dependence, they are complementary with the correlation and phase, which integrate across frequency as a function of time. The coherence and coherence phase are defined as

$$\gamma(f) = \frac{\left\langle \hat{\tilde{X}}\hat{\tilde{Y}}^* \right\rangle^{1/2} \left\langle \hat{\tilde{X}}^*\hat{\tilde{Y}} \right\rangle^{1/2}}{\left|\hat{\tilde{X}}\right|\left|\hat{\tilde{Y}}\right|}$$

$$\delta(f) = \tan^{-1}\left(\frac{\mathrm{Im}\left\langle \hat{\tilde{X}}\hat{\tilde{Y}}^* \right\rangle}{\mathrm{Re}\left\langle \hat{\tilde{X}}\hat{\tilde{Y}}^* \right\rangle} \right)$$

Here $\hat{}$ denotes the Fourier transform and * the complex conjugate of a signal. The correlation and coherence have lower-limits of credibility determined by the size of the ensemble, below which the signals are as disparate as uncorrelated noise. For the coherence this "noise floor" is approximately $1/N^{1/2}$, while for the correlation it is about twice this.[9] Phases calculated where the correlation or coherence fall below this level are meaningless.

2.5 The Toroidal Array and Pseudo-spectral Analysis

In the previous section we found that the limitation of single-point measurements with respect to measuring flux-surface averages can be overcome using time- or event-ensembling techniques. In this section we address another limitation of single-point measurements, namely their inability to provide

spatial frequency information about the fluctuations they measure. This shortcoming can be partly overcome by comparison of a single-point signal with another fluctuating quantity of known mode structure. Fortunately, MST's extensive toroidal array of magnetic coils allows for just such a comparison: the magnetic array can be decomposed into its spatial components, each of which can then be correlated with a single-point signal of interest to provide what will be referred to as a "pseudo-spectrum" for that signal.

For these experiments, the toroidal array of 32 Bt- and 32 Bp-coils were used for pseudo-spectral analysis. The coils are evenly distributed about the machine at angles ϕ_i (i = 1...32), and yield signals B_i (taken as either Bt or Bp). This allows spatial Fourier decomposition into 31 distinct modes, with toroidal mode numbers n = 1...16 for the cosine component and n = 1...15 for the sine component. Thus,

$$\mathbf{B}_{mode} = \mathbf{A}^{-1}\mathbf{B}_{signal}, \text{ where}$$

$\mathbf{B}_{mode} = (B_{equil}, B_{1,cos}, B_{1,sin}, B_{2,cos}, \ldots, B_{15,sin}, B_{16,cos})$ are the sine and cosine mode amplitudes for modes n=1 to n=15 (for sine) or 16 (for cosine), $\mathbf{B}_{signal} = (B_{\phi_1}, B_{\phi_2}, \ldots, B_{\phi_{32}})$ are the signals from the 32 coils of the toroidal array located at angle ϕ_i, and

$$\mathbf{A} = \begin{pmatrix} 1 & 1 & \cdots & 1 \\ \cos(\phi_1) & \cos(\phi_2) & & \cos(\phi_{32}) \\ \sin(\phi_1) & \sin(\phi_2) & & \sin(\phi_{32}) \\ \cos(2\phi_1) & \cos(2\phi_2) & & \cos(2\phi_{32}) \\ \vdots & \vdots & \ddots & \vdots \\ \sin(15\phi_1) & \sin(15\phi_2) & & \sin(15\phi_{32}) \\ \cos(16\phi_1) & \cos(16\phi_2) & \cdots & \cos(16\phi_{32}) \end{pmatrix}$$

is the finite Fourier basis for decomposition. The psuedo-spectrum X_i of a signal X is then given by correlating X with either the sine or cosine component of each mode. (Ideally the sine and cosine components are perfectly correlated, so the choice of cosine versus sine or some combination such as their sum in quadrature is irrelevant. In practice the values do not come out exactly the same, but do give similar spectra and hence the choice does not affect the conclusions drawn from the analysis.) Hence, for i = 1...16,

$$X_i = \mathrm{corr}(\tilde{X}, B_{i,\cos}),$$

$$\mathrm{phase}(X_i) = \mathrm{phase}(\tilde{X}, B_{i,\cos})$$

etc. Due to uncertainties in calibrating the Bp array, the Bt-pseudo-spectrum is more reliable for low n. As will be seen in the next chapter, this is where all the action is in the edge velocity fluctuations, so when not otherwise specified the Bt spectra will be used for this analysis.

REFERENCES

1 G. Fiksel, D. J. Den Hartog, and P.W. Fontana, Rev. Sci. Instrum. **69**, 2024 (1998).

2 J.T. Chapman, Ph.D. thesis, University of Wisconsin–Madison, Madison, 1998.

3 B.A. Trubnikov, *Reviews of Plasma Physics*, Vol. 1 (Consultants Bureau, New York, 1965) p. 105.

4 Chapman, p. 102.

5 D. Craig, Ph.D. thesis, University of Wisconsin–Madison, Madison, 1998, pp. 68*ff.*

6 A.F. Almagri *et al.*, Phys. Fluids B **4**, 4080 (1992).

7 Density measurements compliments of C.-S. Chiang, University of Wisconsin–Madison.

8 Chiang, personal communication, and H. Ji *et al.*, Rev. Sci. Instrum. **62**, 2326 (1991).

9 Chapman, p. 90.

3: *Edge Equilibrium Ion Flows*

3.0 Introduction

The large equilibrium flow profile in the RFP poses an interesting conundrum. One of the most obvious and earliest-observed large-scale phenomena, it remains difficult to account for; explanations range from large but as-yet-unobserved equilibrium electric fields and diamagnetic drifts to fluctuation-induced Reynolds stresses combined with stochastic parallel momentum transport or viscous torques. This work does not claim to unravel the mystery, but the first step in scientific understanding is careful observation. With the IDSP, RFP edge ion (and hence plasma) velocity profiles have been directly measured for the first time, and the results are reported in this chapter.

Section 3.1 covers the toroidal flow profile, particularly as it changes over a dynamo event. The flow is consistent with an $\mathbf{E} \times \mathbf{B}$ drift produced by a radially-outward electric field, and reverses direction when the poloidal magnetic field is reversed. The profile flattens during the crash, with flattening beginning in the core and propagating outward across the reversal surface. In Section 3.2

the poloidal profile is found to be less strongly affected by the sawtooth, although inside the reversal surface the flow gradually accelerates in the wake of the crash. The parallel momentum profile, however, is seen to flatten during the dynamo event. Arguments are presented in Section 3.3 which suggest a radially-inward equilibrium flow. Section 3.4 shows that although biased probes strongly change the toroidal flow profile in the region $0.83 < r/a < 0.94$, they do not change the shear there. Changes in the toroidal flow during poloidal current drive are shown in Section 3.5. The chapter ends with a measurement of the "local safety factor" profile, or field pitch angle, q(r), in the standard discharges studied; the q=0 surface is found to move outward by a little more than 1 cm during the dynamo event.

3.1 Toroidal Velocity Profile

Extensive measurements of the equilibrium toroidal ion velocity profile have been made. Figure 3.1 shows the toroidal ion velocity for a typical shot at an insertion depth of 10 cm (r/a=0.81). The negative sign indicates by convention the direction of decreasing toroidal angle, clockwise from above; this is the same direction as the plasma current and as the core modes. The equilibrium shows changes on two time scales. Over an entire shot, the ions accelerate while the plasma is being driven to a maximum speed on the order of 10 to 20 km/s, and decelerate as the plasma current decays as the discharge ramps down. In addition, rapid changes occur during dynamo events, consisting of a deceleration on the order of 10^7 m/s^2 preceding the crash followed by a similar or slightly slower acceleration afterward. The deceleration at the sawtooth is seen in core IDS measurements and in the toroidal velocity of the core modes.

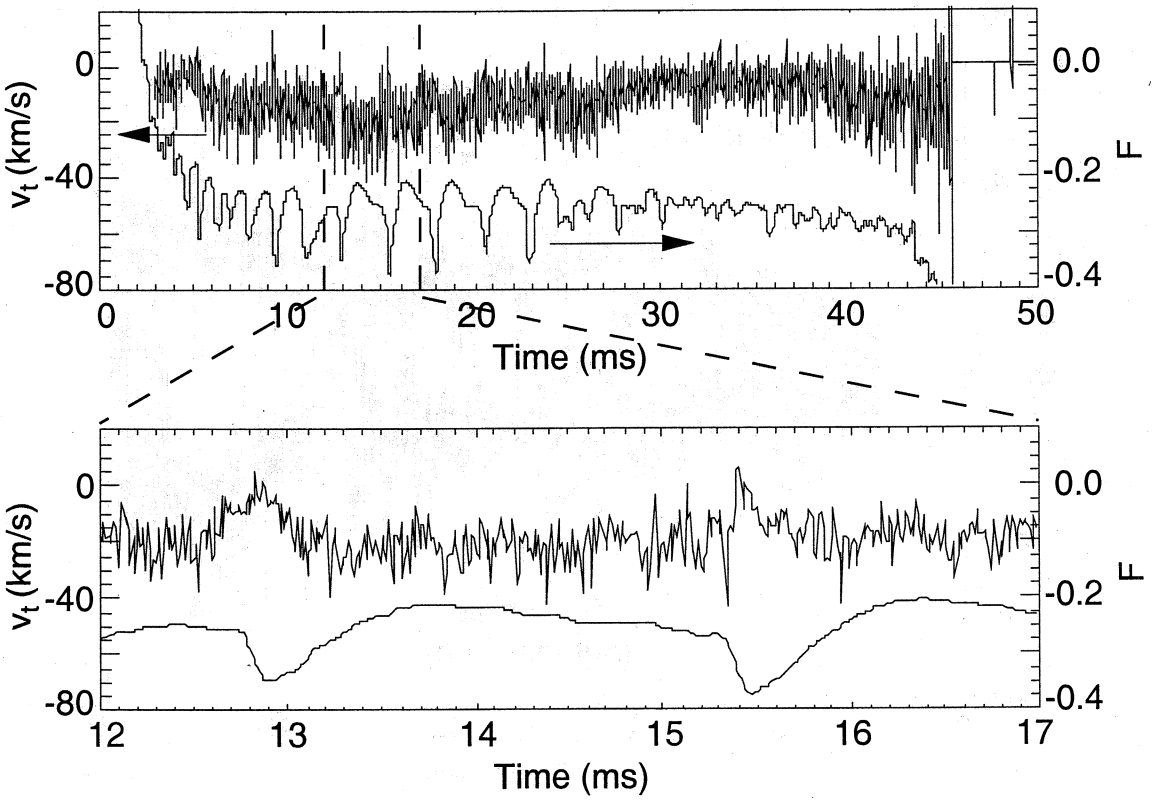

Figure 3.1. Edge Toroidal Ion Velocity for a Typical Discharge. Shown are the IDSP velocity measurement (r/a = 0.81) and the field reversal parameter. Top: The entire discharge. Bottom: Zoom of 12 to 17 ms, showing deceleration at sawteeth.

Some velocity data were taken with the windings of the poloidal field transformer reversed so as to produce a plasma current I_p in the counterclockwise-from-above rather than the usual clockwise direction. This has the effect of reversing the direction of the equilibrium poloidal magnetic field B_p so that it is outboard-down rather than outboard-up. The toroidal velocity measured in this configuration is equal in magnitude but opposite in direction from v_t in normal discharges (Figure 3.2). This observation supports hypotheses which invoke **ExB** or ∇**P**x**B** drifts to explain the equilibrium toroidal flow.

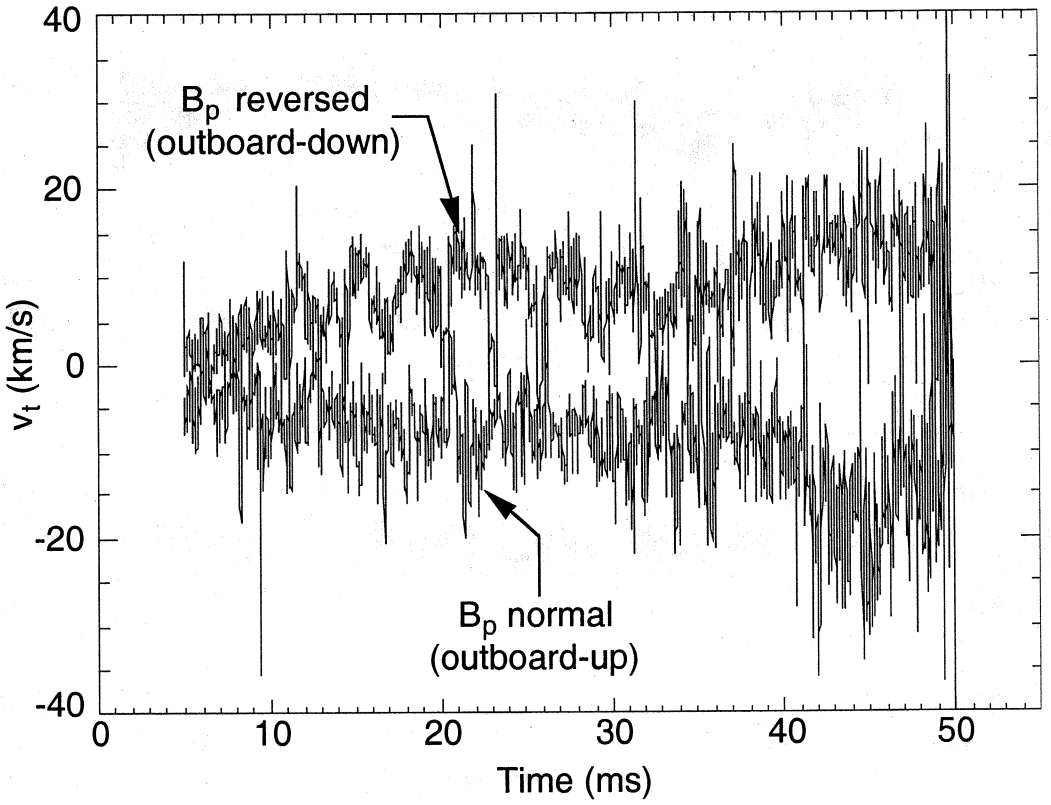

Figure 3.2. Toroidal Ion Velocity with Reversed and Normal B_p. One discharge in each configuration is shown, gently smoothed for clarity. (Shot 56 (normal) and Shot 19 (reversed) on 14 March 1998).

Figure 3.3(a) shows the sawtooth evolution of v_t as a function of radius. Each position shows the toroidal velocity in a 1.0 ms-wide window about the peak of the dynamo event, ensembled over many sawteeth. Figure 3.3(b) shows a subset of this information, with three time slices at each radial position: t = -0.3 ms (asterisks), t = 0.05ms (diamonds), and t = 0.5 ms (triangles) with respect to the crash; multiple ensembles are reperesented at some radii. The profile is linear both away from and at the peak of the sawtooth but exhibits much less shear at the peak.

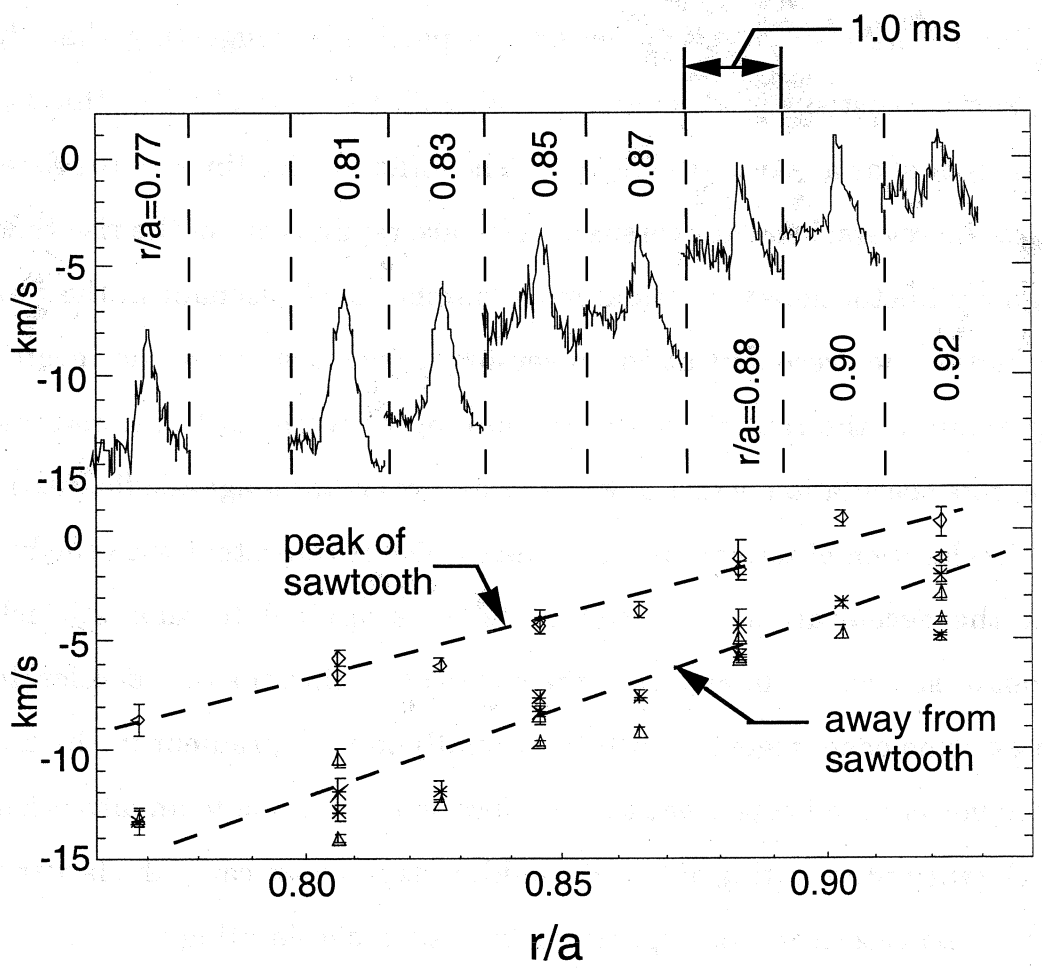

Figure 3.3. Profile of Toroidal Velocity during a Sawtooth. Top: A 1 ms wide sawtooth ensemble window at each insertion. Bottom: Averages around -0.3 ms (asterisks), 0.05 ms (diamonds) and 0.5 ms (triangles) with respect to the sawtooth, showing flattening at the crash.

The details of the time-dependence of the toroidal velocity over a sawtooth are revealing. Because the baseline and the peak of the time trace of velocity are well-defined, the baseline can be subtracted and the data renormalized to the peak value. This removes amplitude information, leaving pure time dependence (Figure 3.4). The results show clearly that the deceleration begins deep and propagates outward through this region. Not only can the direction of propagation of the "sawtooth effect" be determined, but its speed can be estimated at about 4 km/s. The r/a=0.77 and r/a=0.92 ensembles (not shown) are

similar to the r/a=0.81 and r/a=0.88 respectively, suggesting that the effect propagates most slowly through the region of the reversal layer; this region can be thought of as a "sawtooth barrier". The different rise times of the deceleration inside the reversal surface versus outside are reminiscent of the rise times of the magnetic fluctuations of poloidal mode number m=1 resonant in the core versus the m=0 modes resonant at the reversal surface; the lag at the reversal depth may relate to the rate of nonlinear coupling between m=1 and m=0 modes. If true, this speculation would link the locally resonant magnetic fluctuations with the deceleration of toroidal flow, an idea which is consistent with the hypothesis that the deceleration is caused by torques applied to magnetic islands at resonant surfaces.[1] In any case, the observation that the core decelerates before the extreme edge, together with the radially-inward gradient in the magnitude of the velocity, indicates that the deceleration is not due to an advection of flow, which when propagating outward would be expected to carry the larger core flow with it and accelerate the edge flow rather than decelerating it.

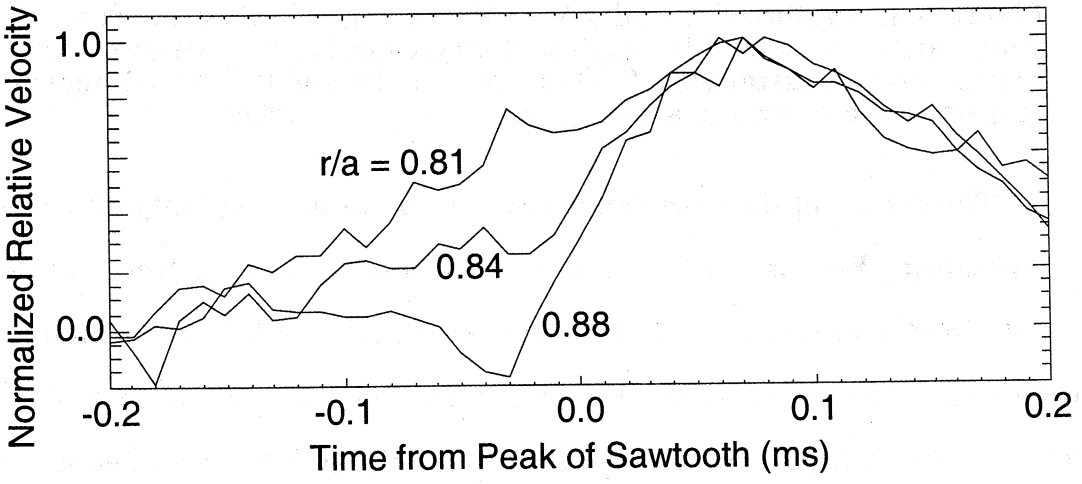

Figure 3.4. Time Dependence of Toroidal Velocity at a Sawtooth. The sawtooth-ensembled velocity with baseline subtracted, then renormalized to its peak value. Measurements for r/a < 0.81 and r/a > 0.88 (not shown) are similar to the extrema shown.

3.2 Poloidal Velocity Profile

The poloidal ion velocity profile exhibits quite different behavior from the toroidal velocity (Figure 3.5). The poloidal velocity stays close to zero while the plasma current rises, then springs free between 8 and 12 ms. This is a common, though not universal, feature of the poloidal velocity; often the "release" is quite discontinuous and coincides with a sawtooth event. The time behavior of the poloidal velocity is much more structured and varies more from shot to shot than the toroidal velocity. Sawtooth crashes sometimes accelerate it, but not strongly. More common is to see bursts of acceleration immediately following the crash, especially at deeper radii. Finally, the poloidal velocity does not seem to change in magnitude or in direction when B_p is reversed.

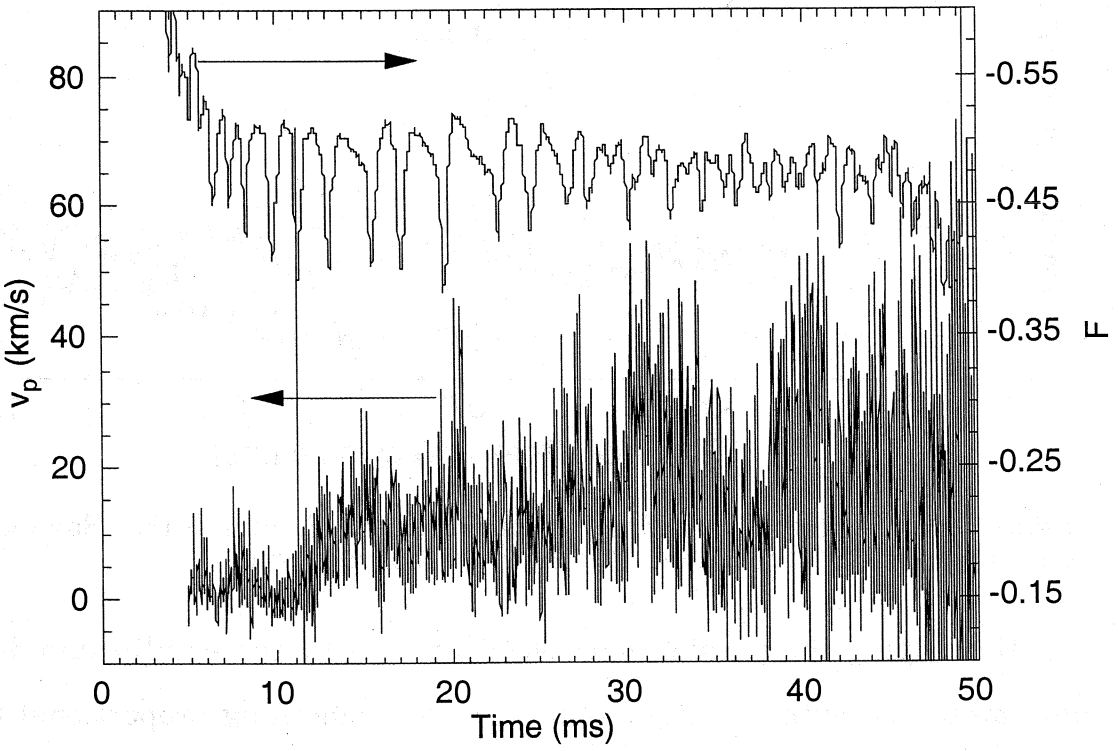

Figure 3.5. Edge Poloidal Ion Velocity for a Typical Discharge. Shown are the IDSP velocity measurement (r/a = 0.81) and the field reversal parameter. For the velocity, positive corresponds to the outboard-down direction.

In profile, the poloidal ion flow is not linear as is the toroidal flow. Instead, its shear is significantly larger in the region of the reversal layer than away from it (Figure 3.6). Also, the v_p profile does not flatten at a sawtooth as does v_t. In fact, the profile steepens across the reversal layer (Figure 3.7), and tends to remain that way during the millisecond after the crash due to its acceleration at smaller radii and perhaps some deceleration at the extreme edge.

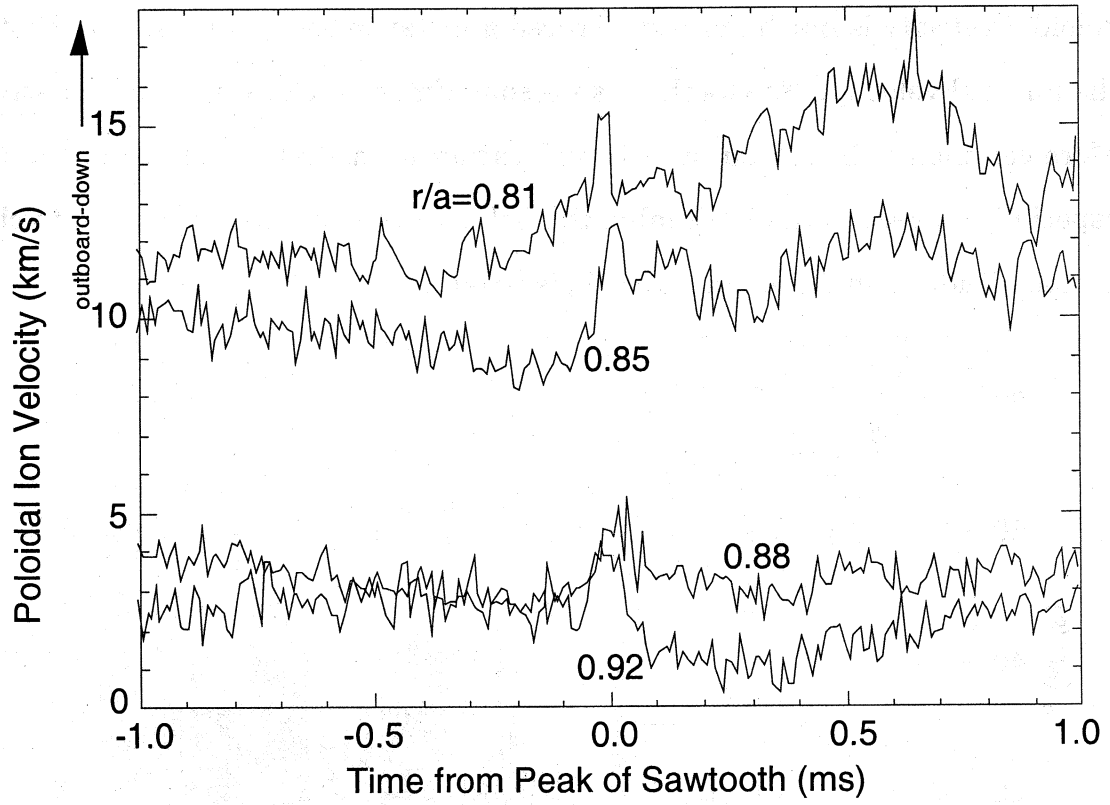

Figure 3.6. Profile of Poloidal Velocity during a Sawtooth (I). Sawtooth ensembles at each insertion. Positive is outboard-down.

Multiplying the parallel ion velocity profile by the equilibrium density profile measured with a Langmuir probe gives something proportional to the parallel momentum profile in MST (Figure 3.8). Since the density profile varies much more strongly versus radius and over a sawtooth than does the velocity, the momentum profile is dominated by the density. The profile is nearly

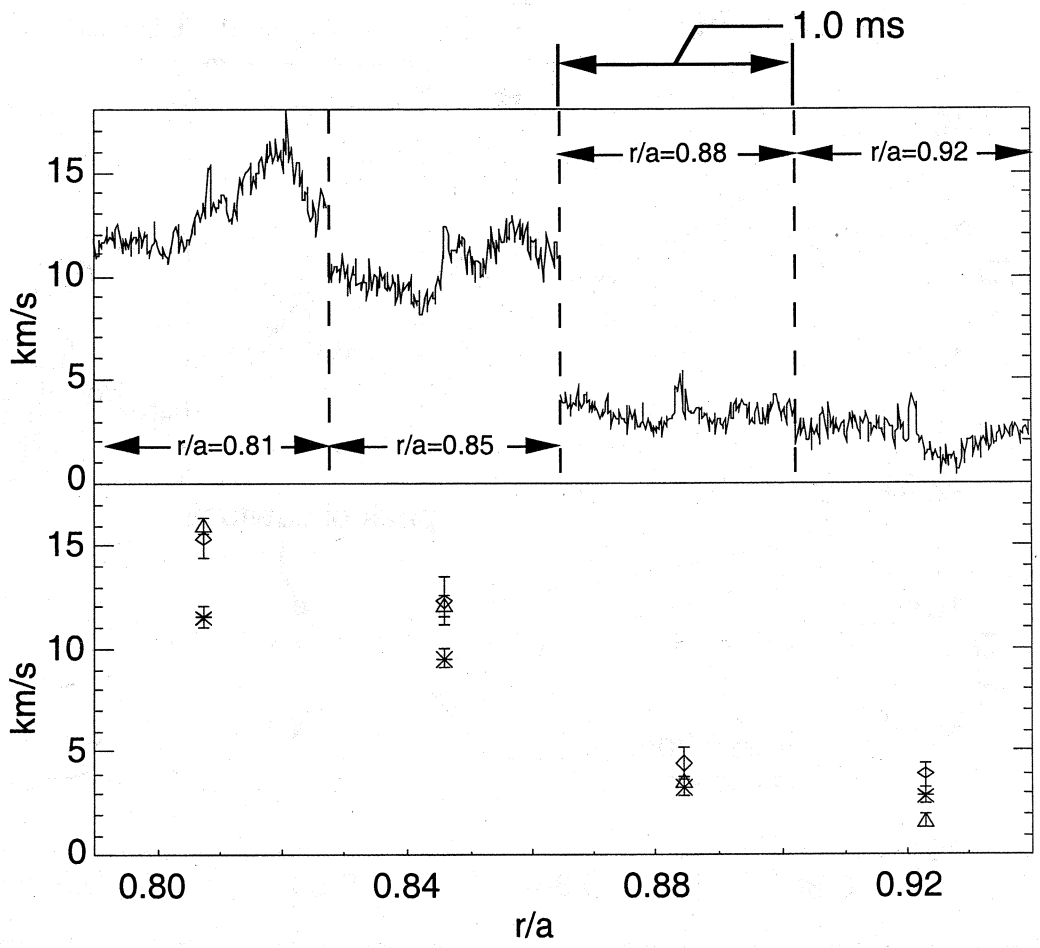

Figure 3.7. Profile of Poloidal Velocity during a Sawtooth (II). Top: A 1 ms wide sawtooth ensemble window at each insertion. Bottom: Averages around -0.3 ms (asterisks), 0.05 ms (diamonds) and 0.5 ms (triangles) with respect to the sawtooth, showing slight but persistent flattening at the crash.

exponential, and is somewhat larger and flatter at the peak of the dynamo event than between sawteeth. This profile change is qualitatively consistent with the theory that parallel momentum should be transported outward during a sawtooth.

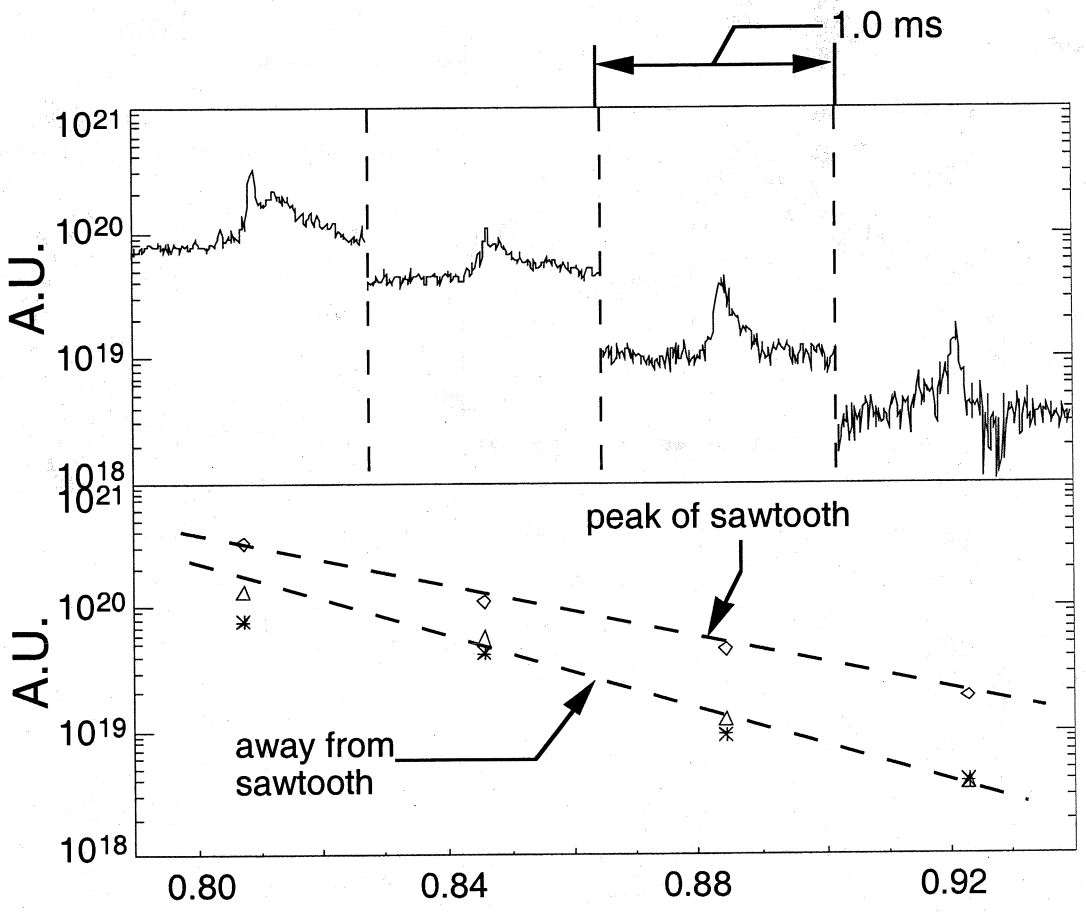

Figure 3.8. Edge Parallel Momentum Profile during a Sawtooth. Shown is $\langle n \rangle \langle v_{||} \rangle$. Top: A 1 ms wide sawtooth ensemble window at each insertion. Bottom: Averages around -0.3 ms (asterisks), 0.05 ms (diamonds) and 0.5 ms (triangles) with respect to the sawtooth, showing flattening at the crash.

3.3 The Case for an Equilibrium Radial Velocity

Due to the geometry of the IDSP, a radial ion velocity produces Doppler shifts of the same sign in both views. As explained in Chapter 2, this means that absolute measurement of radial velocity requires absolute calibration of the spectrometer. This is a luxury not normally available when IDSP data are being taken, so most radial velocity data are accurate only up to an unknown offset. However, even with this limitation it is possible to conclude that there is an equilibrium radial ion flow, at least as measured by the probe. The most

compelling evidence is that the measured radial velocity sometimes changes by as much as 10 or 15 km/s during a shot from its maximum to its minimum (Figure 3.9). Even the most conservative estimate of the offset, which assumes that the average value of v_r is zero during the shot, implies excursions of more than 5 km/s both inward and outward.

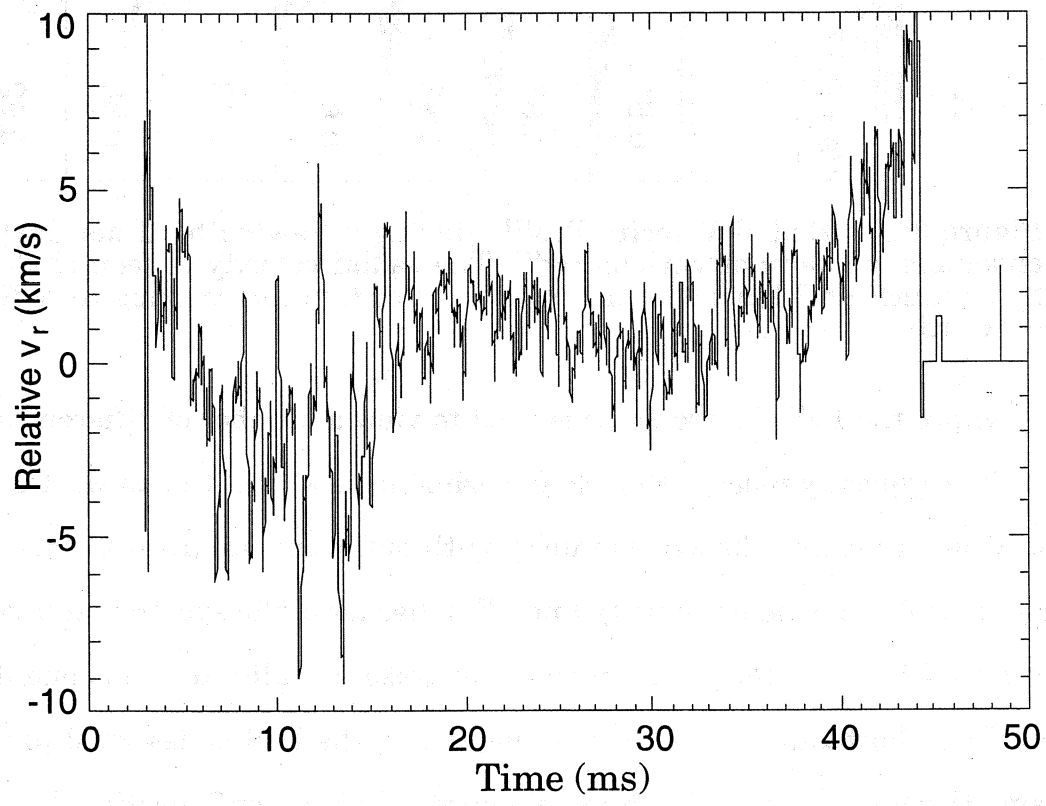

Figure 3.9. Edge Relative Radial Ion Velocity for a Typical Discharge. IDSP measurement at r/a = 0.81. Positive corresponds to radially-outward.

Additional evidence for equilibrium radial flow comes from sawtooth ensembles, which show a consistent change in $\langle v_r \rangle$ during the crash of more than 2 km/s at the deepest radii measured. The change $\partial v_r / \partial t$ is radially outward before the crash and radially inward afterward (Figure 3.10).

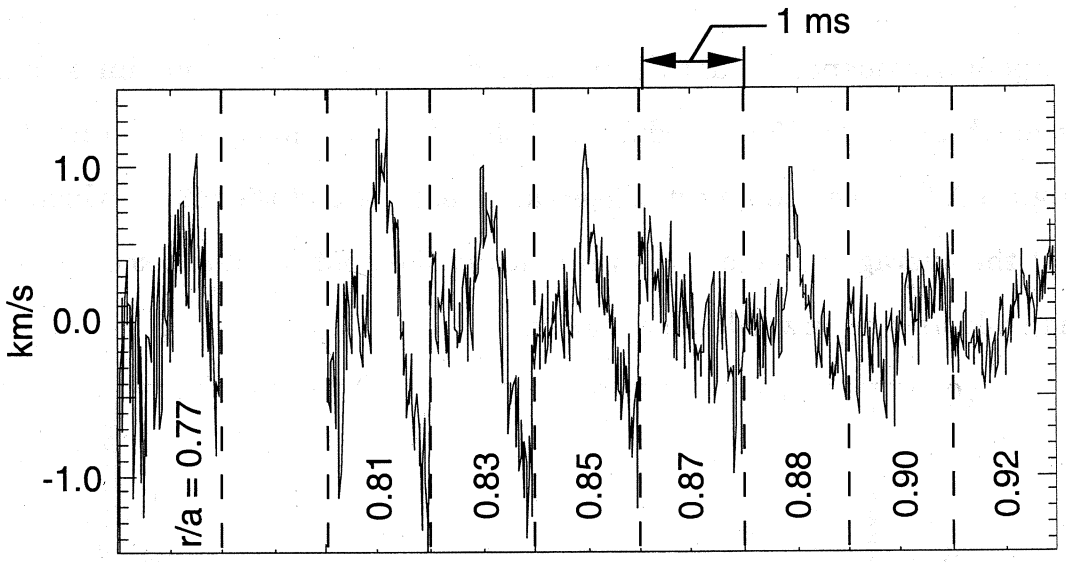

Figure 3.10. Radial Velocity Profile during a Sawtooth. 1 ms sawtooth ensemble windows at various radii. The radial velocity is seen to change by as much as 3 km/s over a sawtooth. Positive corresponds to radially-outward.

Since the IDS spectrometer is used to view a number of different impurity lines, it is typically reset with each experiment in which it is used. Its position in wavelength cannot be set manually with sufficient accuracy to measure the Doppler shift of a single impurity line. Furthermore, the spectrometer setting is known to drift with time, so even when an absolute calibration is done it is only valid for a short time. In its conventional use, the IDS is designed to view the plasma through two opposing toroidal chords. In this configuration, light that is blue-shifted in one view is red-shifted in the other. This design feature is intended to obviate the need for an absolute calibration of the spectrometer offset; it can also be used, however, to perform the calibration itself, since the average position of the two shifted lines is exactly the position of the unshifted line.

Since the conventional IDS configuration and the IDSP cannot be used simultaneously, applying this calibration to IDSP data requires changing from

one configuration to the other without disturbing the spectrometer setting. Because of the drift in the spectrometer, the calibration data and the IDSP data must be taken within a short time of one another, and the calibration must be repeated frequently. This has been done for the purpose of measuring the equilibrium radial plasma flow. Figure 3.11 shows the unshifted position, relative to the 10 Å-wide viewing window of the spectrometer, of the HeII 4685.7 Å line used for IDSP measurements, seen in second order. The position is shown as a function of real time, indicating the spectrometer's drift over the course of the run. The drift is quite linear, so the unshifted position can be interpolated to times between calibrations and applied to IDSP data taken then. If unaccounted for, the total drift throughout the run would correspond to a change in velocity of about 5 km/s

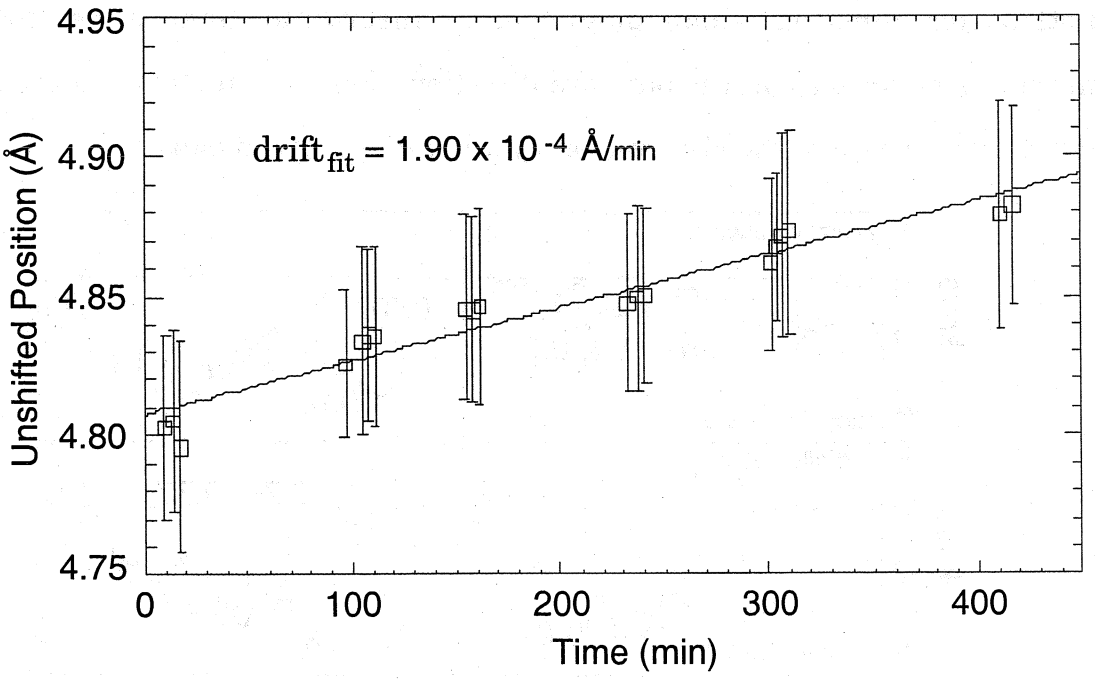

Figure 3.11. Absolute Spectrometer Calibration. Shown is the position of the unshifted HeII 4685.7 Å emission line relative to the 10 Å view of the spectrometer as a function of real running time. Error bars are standard deviations of whole-shot averages.

The result is perplexing. The He ions have a significant equilibrium radial velocity *inward* (Figure 3.12), which is smallest at the most extreme radii but larger and fairly uniform from r/a=0.77 to 0.87, displaying similar time-dependence after about 20 ms into the shot. The equilibrium v_r does not fluctuate around zero, but remains inward, tapering off to zero at the end of the shot. We have not identified a plasma phenomenon which would produce such a pinch. That the effect is weaker at the extreme edge contraindicates a porthole-induced field error as the cause, since the effect of this should be stronger at shallower insertions. At deep insertions the probe has been seen to slow mode rotation on a time scale similar to the rise in $\langle v_r \rangle$; this, together with the lack of other adequate explanation, leads to suspicions of plasma-probe interactions as the cause. However, finite Larmor radius effects and depletion of the distribution function which plague other insertable diagnostics should, if anything, enhance v_r in the outward direction. For now, further understanding awaits verification of the observation by other diagnostic means.

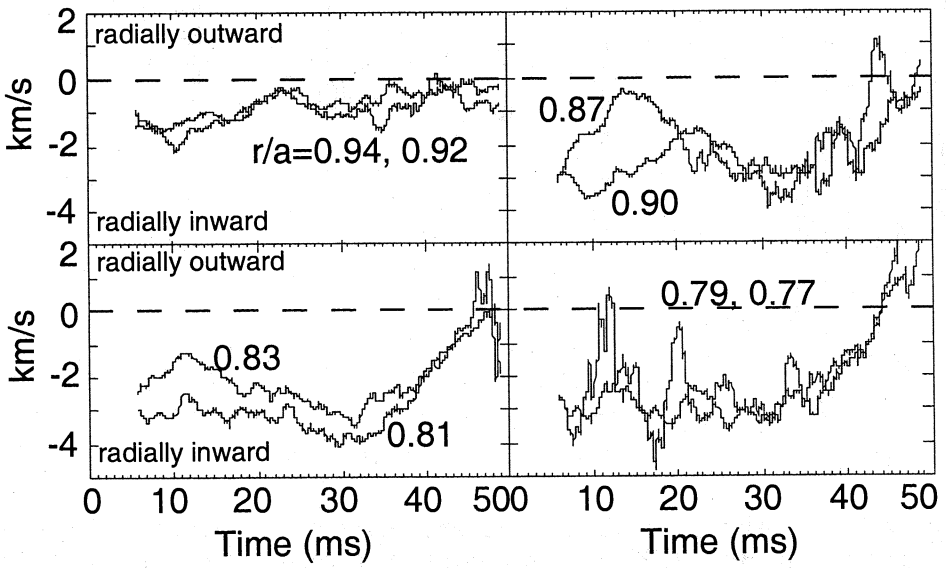

Figure 3.12. Ensembled Radial Velocity Profile. Shown are multiple-shot ensembles of $\langle v_r \rangle$.

3.4 Equilibrium Flows during Electrostatic Current Injection

Theory[2,3] and experimental observation in other types of toroidal fusion plasmas[4] have shown the favorable effect of plasma flow shear on confinement. Meanwhile, experiments have been performed on MST which demonstrate modestly to greatly improved particle and energy confinement under various conditions, though the mechanism of confinement improvement is not always clear; hence the usefulness of diagnosis of the toroidal plasma flow profile during these discharges, made possible by the IDSP. These efforts to improve particle and energy confinement have included a series of experiments using electrostatic current injection probes, or "plasma guns," to enhance the plasma current profile at the edge.[5,6] The result is greatly enhanced particle confinement, apparently due to gun biasing rather than current injection *per se*, and moderately improved energy confinement. One explanation for the improved confinement says that the radial electric field profile is altered by the large bias on the guns in such a

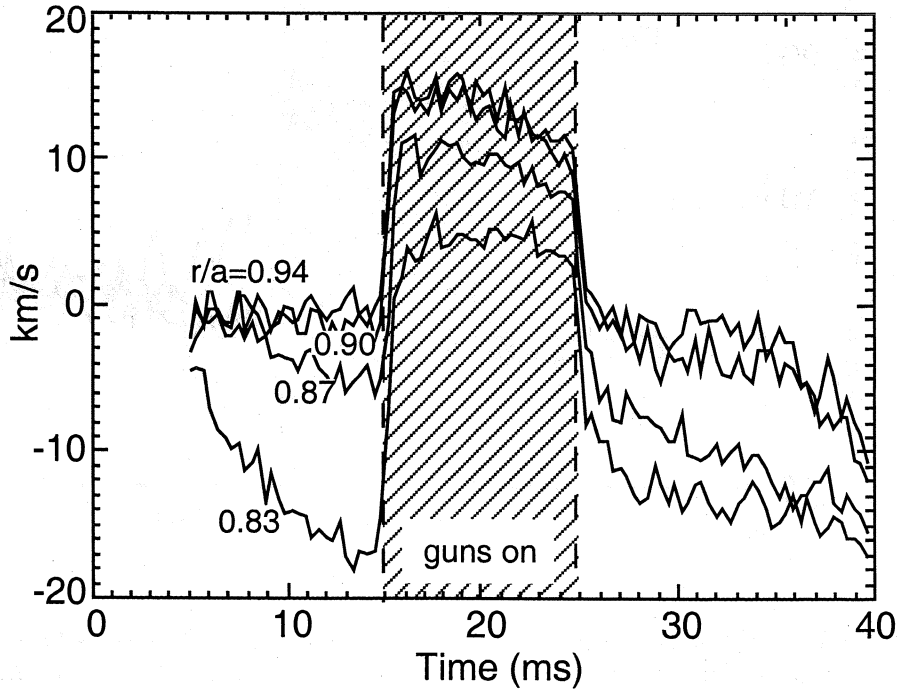

Figure 3.13. Toroidal Flow Profile during Gun Biasing.

way as to increase ***E*x*B*** flow shear in the edge.

The IDSP has been used in gun-biased plasmas to measure the toroidal flow profile. It is seen (Figure 3.13) that during the time that the guns are firing the toroidal flow is quickly and strongly affected, even to the point of reversing direction in the edge. When the bias is turned off again, the plasma flow quickly returns to its unbiased state. To determine the change in shear due to biasing as distinct from the change in shear over time in normal discharges, shots with guns firing were alternated with shots with the guns inserted but off, and the two sets of ensembles were compared. By subtracting the flow profile with guns off from the flow profile with biasing, the change in the flow due to the guns can be seen (Figure 3.14). The result is that the guns boost the toroidal velocity uniformly by about 15 km/s, but the shear measured during current injection is

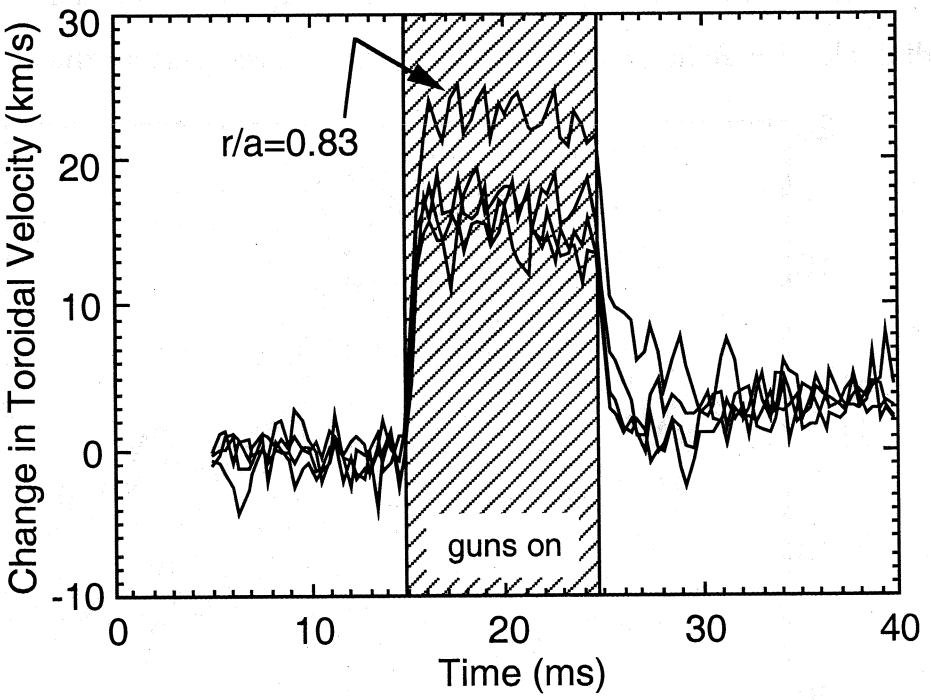

Figure 3.14. Relative Shear with Gun Biasing. Shown is the flow with biasing minus the flow with no bias. The shear does not change in this region with bias.

almost identical to the shear without it. At the deepest insertion measured (r/a=0.83), the flow was boosted slightly more than at larger radii, but this difference is in the direction of flattening the flow profile. If the enhanced confinement due to the guns is a result of increased flow shear, the increase does not occur in this region of the plasma.

3.5 Flow Changes during PPCD

Another current drive scheme, called "pulsed poloidal current drive" (PPCD), uses an external poloidal drive in the sense to flatten the parallel current profile.[7] This scheme currently holds the world record for RFP confinement. Efforts were undertaken to measure the toroidal flow profiles in these discharges to determine the role of flow shear (and dynamo) in the improved confinement. Unfortunately, good confinement in PPCD discharges is sensitive to plasma conditions, and achieving good confinement PPCD with the IDSP inserted deeply proved impossible. However, with the probes at r/a = 0.92 sustained periods of good confinement were produced, and the toroidal velocity showed some consistent changes (Figure 3.15). There is a quick acceleration followed by a gradual deceleration coincident with the onset of PPCD. Then, when good confinement sets in, the plasma accelerates, while the velocity fluctuations decrease. With the end of good confinement the fluctuations return to their former level and the plasma continues to accelerate.

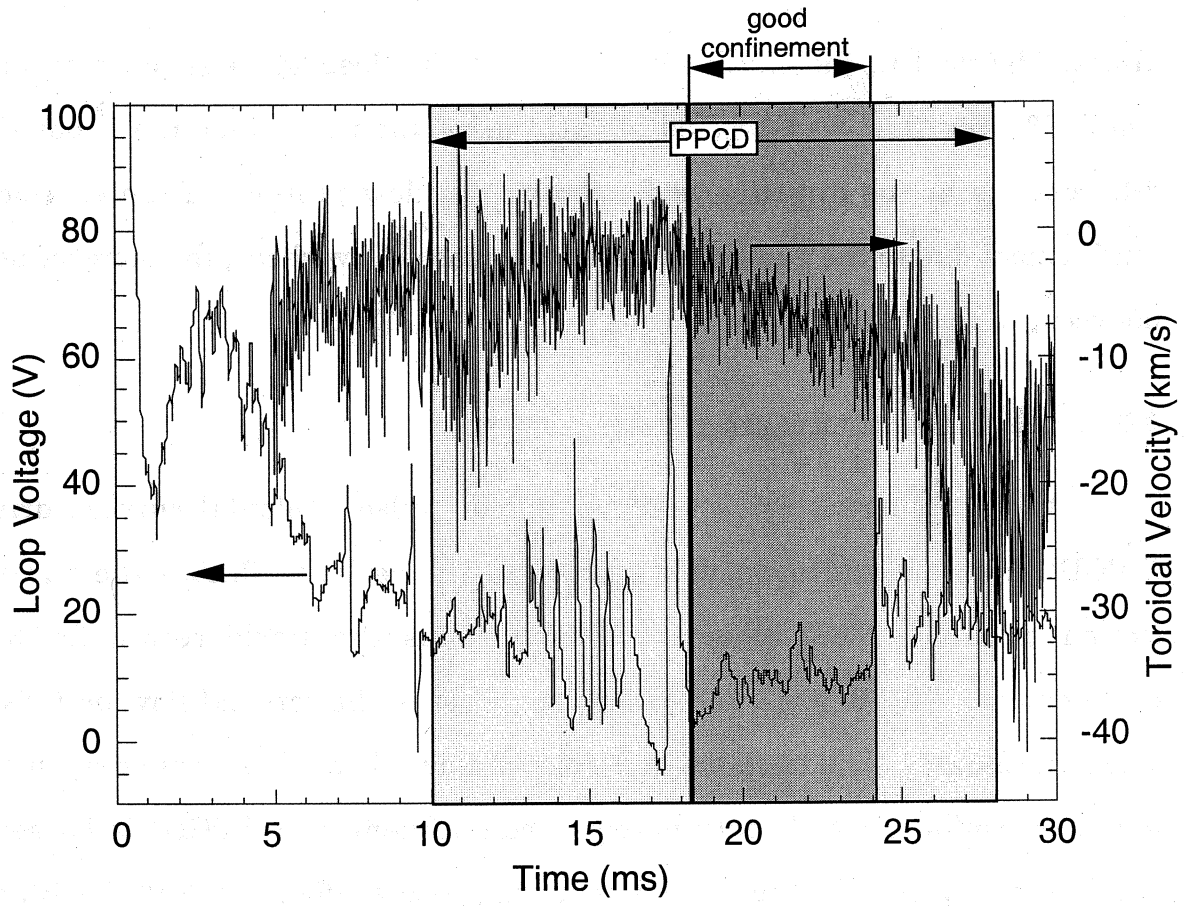

Figure 3.15. Toroidal Velocity during PPCD. Shown are toroidal velocity at r/a = 0.92 and toroidal loop voltage during a typical improved-confinement PPCD discharge. PPCD begins at 10.0 ms and good confinement lasts from shortly after 18 ms to 24 ms.

3.6 Safety Factor Changes and Flow Profiles

An important question to address is whether or not the IDSP samples the same flux surfaces throughout the sawtooth cycle, during which transport is high and the flux surfaces are expected to be in rapid radial motion. Strong changes in quantities of interest measured by the IDSP may be due to changes within the flux-surface or motion of the flux surface with respect to the IDSP. Some sense of this flux-surface motion can be inferred by looking at the local safety factor profile.

The local safety factor q(r) is given by

$$q(r) = \frac{r}{R}\frac{B_t(r)}{B_p(r)}.$$

The magnetic fields $B_t(r)$ and $B_p(r)$ have been measured thoroughly in the edge of the plasmas studied in this thesis using insertable magnetic probes. The sawtooth-ensembled data indicate constant shear ($\partial q/\partial r$) from r/a=0.80 to 1.00 away from a sawtooth, and an abrupt increase in shear near the peak of the sawtooth (Figure 3.16). The profile gradually begins to flatten beginning at the extreme edge. The reversal (q=0) surface, meanwhile, can be interpolated from the data fairly precisely (Figure 3.17). It is seen to move outward during the crash from r/a of about 0.85 to r/a of about 0.87, a swing of about 1 cm. The implication is that the region of view of the IDSP does not change position

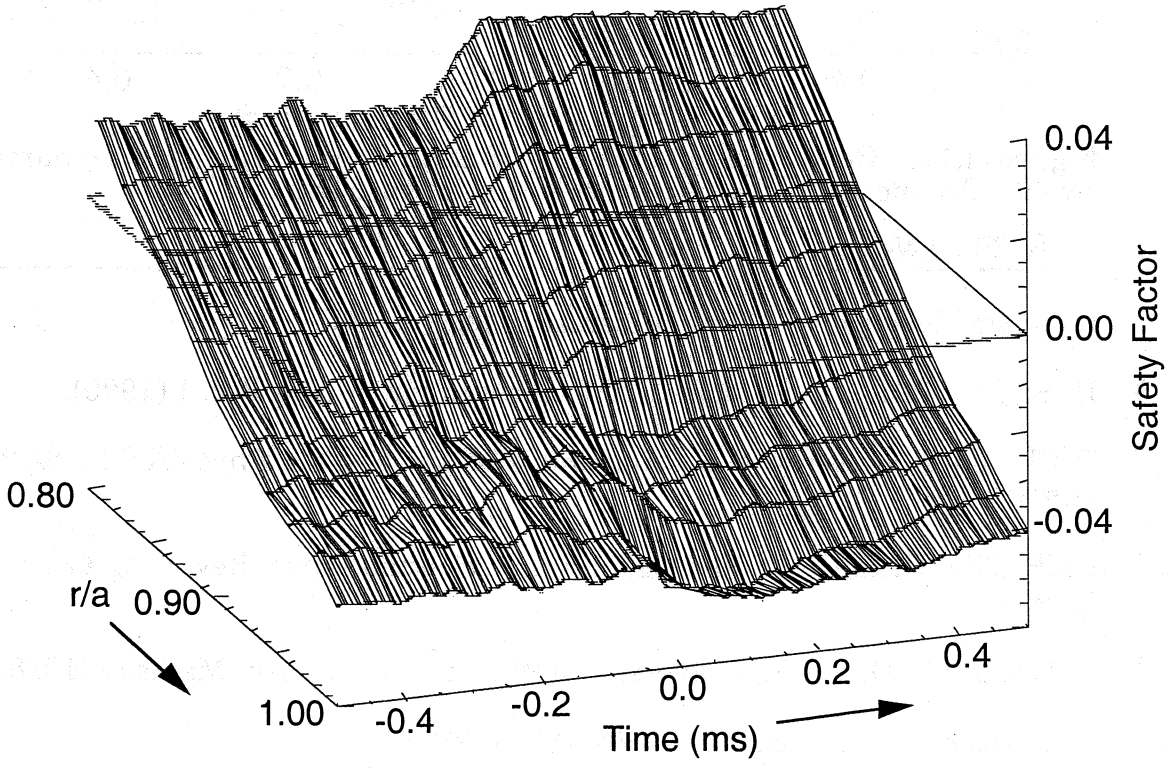

Figure 3.16. Local Safety Factor Profile during a Dynamo Event. The profile steepens at the crash.

radially over a sawtooth by more than about 1 cm in the reference frame of the flux surfaces.

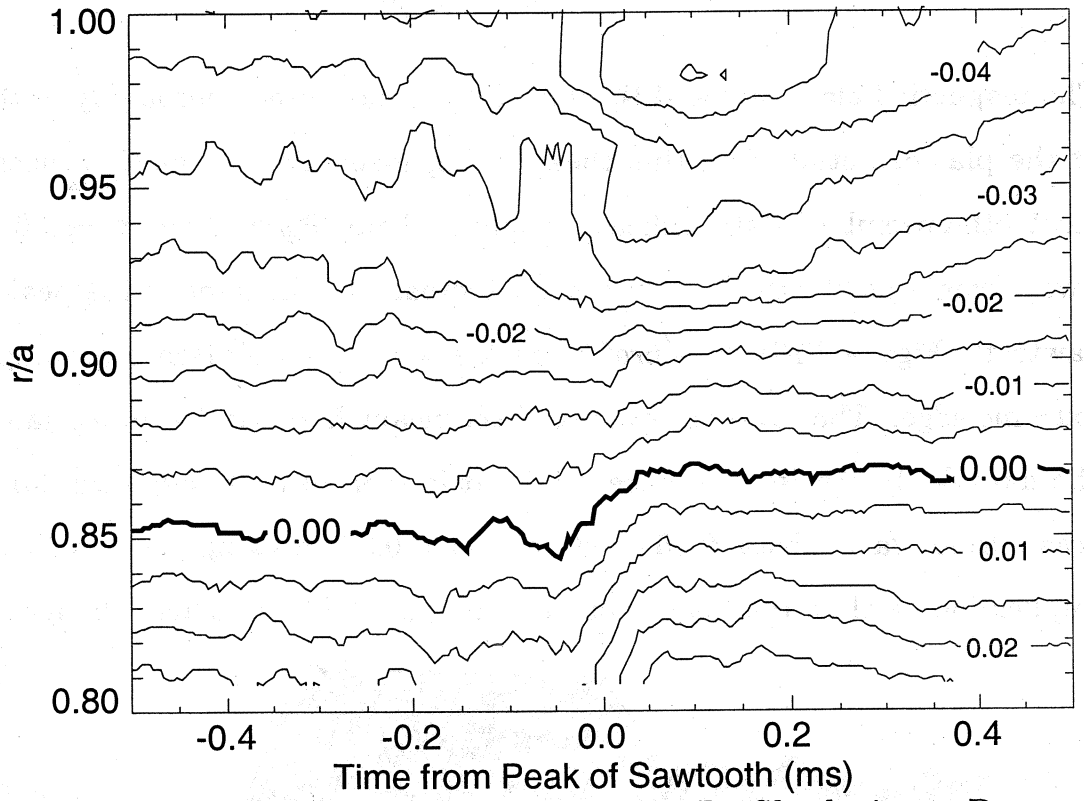

Figure 3.17. Contour Plot of Safety Factor Profile during a Dynamo Event. The motion of the q = 0 surface is emphasized.

REFERENCES

1 D.J. Den Hartog *et al.*, Phys. Plasmas **2**, 2281 (1995).

2 H. Biglari, P.H. Diamond, and P.W. Terry, Phys. Fluids B **2**, 1 (1990).

3 T. Chiueh, P.W. Terry, P.H. Diamond, and J.E. Sedlak, Phys. Fluids **29**, 231 (1986).

4 Ch.P. Ritz, H. Lin, T.L. Rhodes, and A.J. Wootton, Phys. Rev. Lett. **65**, 2543 (1990).

5 D. Craig, Ph. D. thesis, University of Wisconsin–Madison, Madison (1998).

6 D. Craig*et al.*, Phys. Rev. Lett. **79**, 1865 (1997).

7 M.R. Stoneking, N.E. Lanier, S.C. Prager, J.S. Sarff, and D. Sinitsyn, Phys. Plasmas **4**, 1632 (1997).

4: *Edge Velocity Fluctuations and the Dynamo*

4.0 Introduction

The primary effort of this work is the study of the plasma flow velocity fluctuations in the edge of the RFP, in particular their role in the RFP dynamo process. The measurements and results are described in this chapter. As motivation we begin by deriving the single-fluid parallel Ohm's law for the plasma, arriving at a relation involving the dynamo which can be tested experimentally. There follows a description of the measurements of the various terms. A comparison relative to flux-generating sawteeth reveals good time-dependent agreement at radii outside the reversal surface; the dynamo balances the current in the absence of induced electric field away from the sawtooth, then becomes large relative to the current as it balances the large induced e.m.f. as the flux changes. At radii inside of reversal the agreement is not as good, due to the competing effects of the $\tilde{v}_r$ and $\tilde{v}_t$ contributions to the dynamo. Whether this is due to limitations of the measurements or to other mechanisms which can drive current away from the dynamo event and suppress it at the crash awaits future study.

Then, the structure of the edge fluctuations is considered. The velocity fluctuations contributing to the dynamo in this region are analyzed to determine their mode spectrum, revealing a large m=0, n=1 and 2 contribution; there is also slight high-n (~11-14) contribution, corresponding to m=1 activity, inside the reversal surface. This result supports other findings which suggest that the eigenfunctions of the magnetically-correlated part of the velocity fluctuations are much more localized than the eigenfunctions of the magnetic modes.

In addition, the phase of the velocity fluctuations has been measured across their resonant surface, which in the case of these m=0 modes is the reversal surface. The fluctuations display tearing-mode parity, with $\tilde{v}_r$ flipping phase across the resonant surface while $\tilde{v}_t$ does not. These results are reported in the final section.

4.1 Mean-Field Ohm's Law

In this section the generalized mean-field Ohm's law is derived from a two-fluid plasma description.[1] Assuming a plasma of electrons (indicated by the subscript 'e') and singly-ionized ions (indicated by 'i'), the equations of motion of the species are

$$nm_i\left(\frac{\partial \mathbf{v}_i}{\partial t} + \mathbf{v}_i \cdot \nabla \mathbf{v}_i\right) = ne\left(\mathbf{E} + \mathbf{v}_i \times \mathbf{B}\right) - \nabla p_i + \mathbf{P}_{ie}$$

$$nm_e\left(\frac{\partial \mathbf{v}_e}{\partial t} + \mathbf{v}_e \cdot \nabla \mathbf{v}_e\right) = ne\left(\mathbf{E} + \mathbf{v}_e \times \mathbf{B}\right) - \nabla p_e - \mathbf{P}_{ie},$$

where $\mathbf{P}_{ie}$ is the drag of the electrons on the ions, n is the electron and ion density (quasineutrality has been assumed), m is mass, $\mathbf{v}$ is each species' fluid velocity, $\mathbf{E}$ is the electric field, $\mathbf{B}$ the magnetic field, and p the pressure (where

the stress tensor has been assumed to be diagonal and isotropic). Defining the single-fluid quantities

$$\rho = n(m_i + m_e)$$
$$\mathbf{v} = \frac{m_i \mathbf{v}_i + m_e \mathbf{v}_e}{m_i + m_e}$$
$$\mathbf{j} = en(\mathbf{v}_i - \mathbf{v}_e)$$
$$\mu = \frac{m_i m_e}{m_i + m_e},$$

subtracting $\partial \mathbf{v}_e/\partial t$ from $\partial \mathbf{v}_i/\partial t$, and multiplying by μ/e gives

$$\frac{\mu}{ne^2}\frac{\partial \mathbf{j}}{\partial t} = \mathbf{E} + \mathbf{v}\times\mathbf{B} - \eta\mathbf{j} + \frac{1}{e\rho}\left[m_i \nabla p_e - m_e \nabla p_i - (m_i - m_e)\mathbf{j}\times\mathbf{B}\right],$$

where it has been assumed, as is reasonable, that $\mathbf{P}_{ie} \propto -\mathbf{j}$, and the resistivity η has been defined such that $\mathbf{P}_{ie} = -en\eta\mathbf{j}$; also, quantities which are quadratic in velocity have been ignored. This equation is referred to as the "generalized Ohm's law".

Adding $m_i \partial \mathbf{v}_i/\partial t$ to $m_e \partial \mathbf{v}_e/\partial t$ gives an expression for $\mathbf{j} \times \mathbf{B}$, to wit,

$$\mathbf{j}\times\mathbf{B} = \rho\frac{\partial \mathbf{v}}{\partial t} + \nabla p_e + \nabla p_i,$$

which when substituted into the generalized Ohm's law gives

$$\mathbf{E} + \mathbf{v}\times\mathbf{B} = \eta\mathbf{j} + \frac{1}{e\rho}(m_e \nabla p_e - m_i \nabla p_i) + \frac{1}{e}\frac{\partial}{\partial t}\left[\frac{\mu}{ne}\mathbf{j} - (m_i - m_e)\mathbf{v}\right].$$

With the assumption (already used in Chapter 2 to justify ion spectroscopy) that $m_i v_i >> m_e v_e$, the terms in the final time derivative are dominated by $\frac{m_i}{e}\frac{\partial \mathbf{v}}{\partial t}$. Comparing this term to the $\mathbf{v} \times \mathbf{B}$ term and anticipating that we will ultimately only be interested in the parallel component, we compare the magnitudes $\tilde{v}\tilde{b}$

and $\frac{m_i}{e}\frac{\partial v_\parallel}{\partial t}$. Since $v_\parallel$ and $\tilde{v}$ are measured to be of the same order, we find that the time derivative is only significant on time scales ω such that

$$\omega \geq \omega_{ci}\frac{\tilde{b}}{B}\gamma\cos\delta,$$

where ω_{ci} is the ion cyclotron frequency, and γ and $\cos\delta$ are the correlation and phase between $\tilde{v}$ and $\tilde{b}$. Using the measured magnetic fluctuation amplitude of 2.5% and typical $\gamma\cos\delta$ of 50% gives a lower limit of about 100kHz on ω. We conclude, then, that on the time scales of interest here (~10kHz), the entire $\partial/\partial t$ term, including the Hall effect (from $\mathbf{j}\times\mathbf{B}$), is small compared with $\mathbf{v}\times\mathbf{B}$; for now it will be neglected, with a note in passing that the term may regain importance as a current drive in Ohm's law in such situations where the dynamo becomes insignificant. Then the parallel component of Ohm's law, assuming that pressure gradients are small in this direction and pressure waves do not contribute, becomes

$$E_\parallel + (\mathbf{v}\times\mathbf{B})_\parallel = \eta j_\parallel.$$

Separating quantities into mean-field and fluctuating parts and averaging over a flux surface as described in Chapter 2, we have

$$\langle E\rangle_\parallel + \langle\tilde{\boldsymbol{v}}\times\tilde{\boldsymbol{b}}\rangle_\parallel = \eta\langle j\rangle_\parallel.$$

This is the simple form of Ohm's law to be studied in this work. The term $\langle\tilde{\boldsymbol{v}}\times\tilde{\boldsymbol{b}}\rangle$, representing as it does an electric field arising from fluctuations in the flow of a conducting fluid in the presence of a magnetic field, will be referred to as the fluctuation-induced dynamo. Henceforth the angled brackets will be dropped from mean-field quantities except where necessary to prevent ambiguity. All of

the quantities in this equation have been measured or estimated, as described in the following sections.

4.2 Induced Parallel Electric Field Measurement

The induced electric field profile, $E_{||}(r)$, was obtained from the poloidal surface loop voltage (toroidal gap voltage) V_{tg} corrected for the flux change inside the torus but outside the radius of the electric field measurement (Figure 4.1); thus,

$$E_{||}(r) = \frac{V_{tg}}{2\pi r} - \frac{1}{r}\frac{\partial}{\partial t}\int_r^a B_t(r')\,r'\,dr' .$$

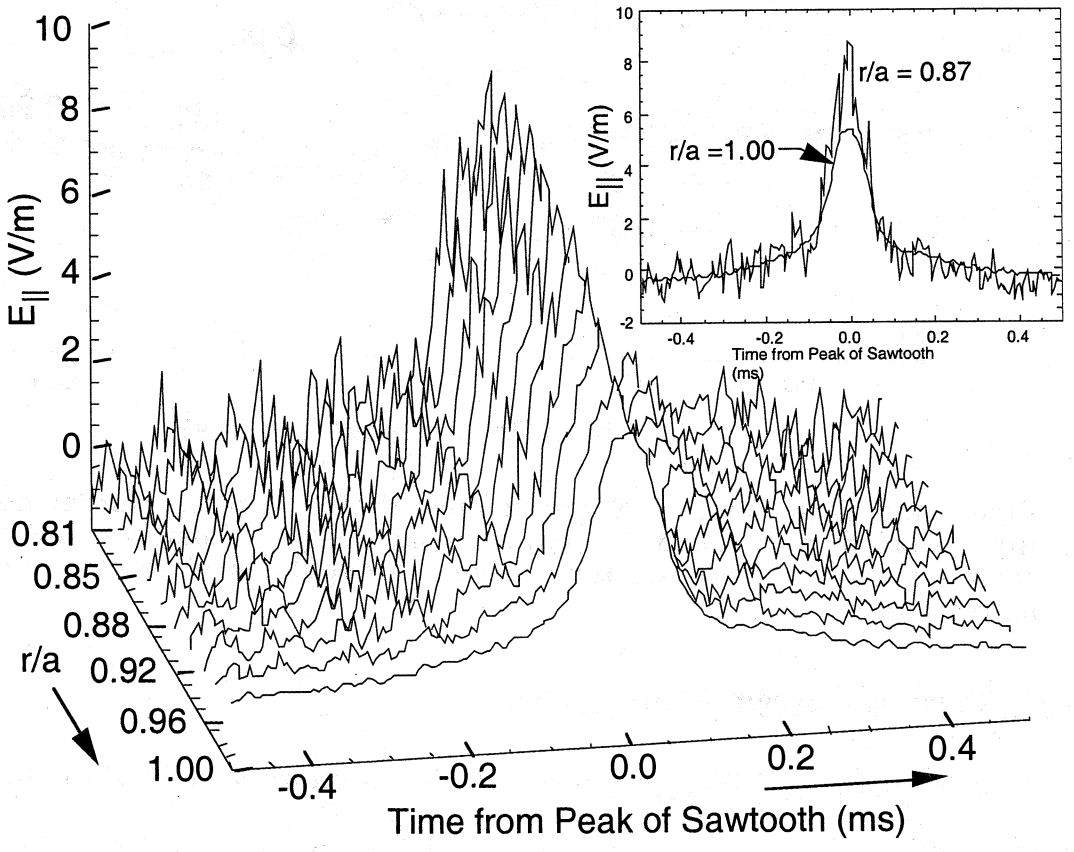

Figure 4.1. Edge Parallel Electric Field Profile. Shown is $E_{||}$ over a sawtooth in the range $0.80 < r/a < 1.00$. Positive indicates the outboard-up direction. The inset shows the value at the radii where the extrema are achieved. Small fluctuations are probably artifacts from finite ensembles and represent the uncertainty.

The $B_t(r)$ profile was determined from the magnetic signals from the Rogowski probe described in Chapter 2, and circular, axially symmetric flux surfaces have been assumed (Figure 4.2). The measurement was ensembled over 85 to 125 similar sawteeth (about half as many for ensembles at r/a < 0.84).

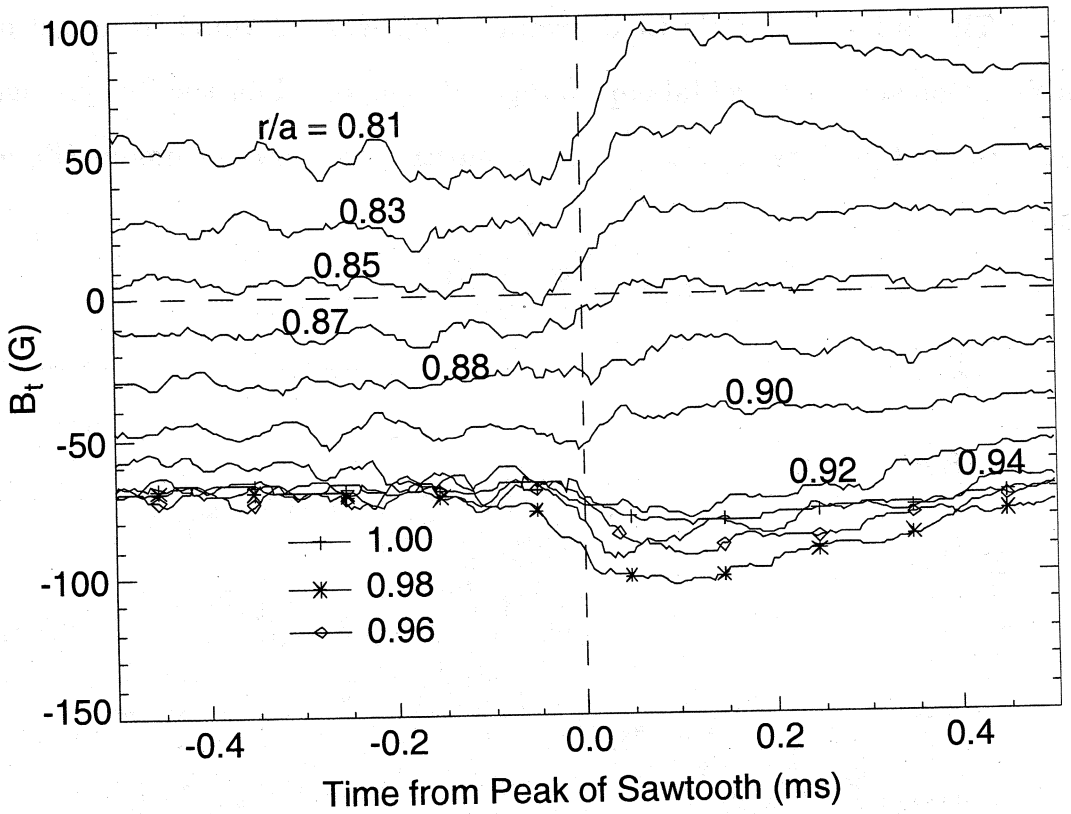

Figure 4.2. Edge Toroidal Magnetic Field Profile. The measurements are interpolated and used in calculating $E_{||}(r)$. Positive indicates counterclockwise from the top. Note the expulsion of toroidal flux at extreme radii.

4.3 Parallel Current Measurement

The current profile, $j_{||}(r)$, was obtained simultaneously with the electric field profile using the insertable Rogowski probe (Figure 4.3). The plasma resistivity η was not directly measured, since measurements of local effective ion charge state Z_{eff} were not available. However, at the low electron temperature

(< 50eV as measured by Langmuir probes) of the edge plasma in MST, the probability of stripping impurity ions to high charge states is small; hence a Z_{eff} as high as 2 is unlikely. For the present comparison, then, a Z_{eff} of 1.5 has been assumed and η is calculated from Spitzer's formula[2]. Since the contribution of the current term in Ohm's law is modest, the uncertainty in the estimated resistivity does not affect the conclusions which follow.

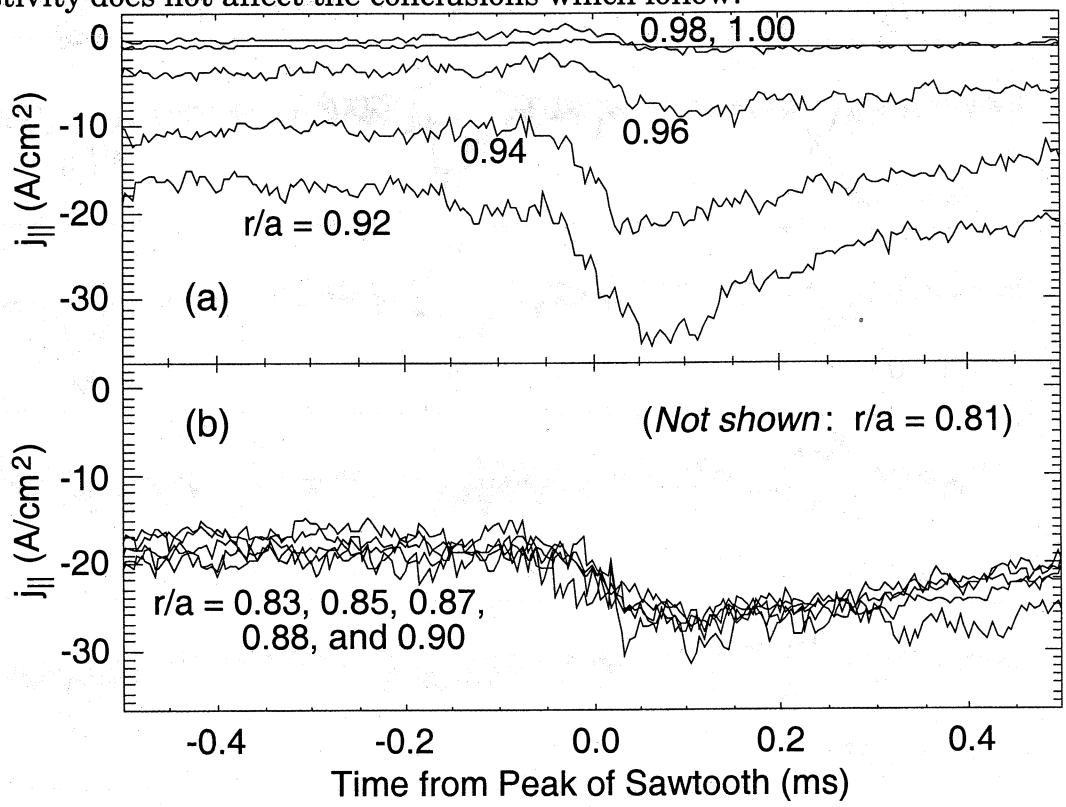

Figure 4.3. Edge Parallel Current Profile. (a) The profile rises steeply from the wall to a maximum at r/a = 0.92. (b) The profile is flat from r/a = 0.90 in to r/a = 0.81. The deepest measurement is similar to those in (b) but with larger variation, probably due to its smaller ensemble, and is left off for clarity. The negative sign indicates the outboard-down direction.

4.4 Profile of the Fluctuation-Induced Dynamo and Ohm's Law

The parallel component of the fluctuation-induced dynamo $\langle \tilde{\boldsymbol{v}} \times \tilde{\boldsymbol{b}} \rangle_{||}$ is comprised of two constituent terms: $\tilde{v}_r \tilde{b}_t$ and $\tilde{v}_t \tilde{b}_r$. Using the IDSP and the

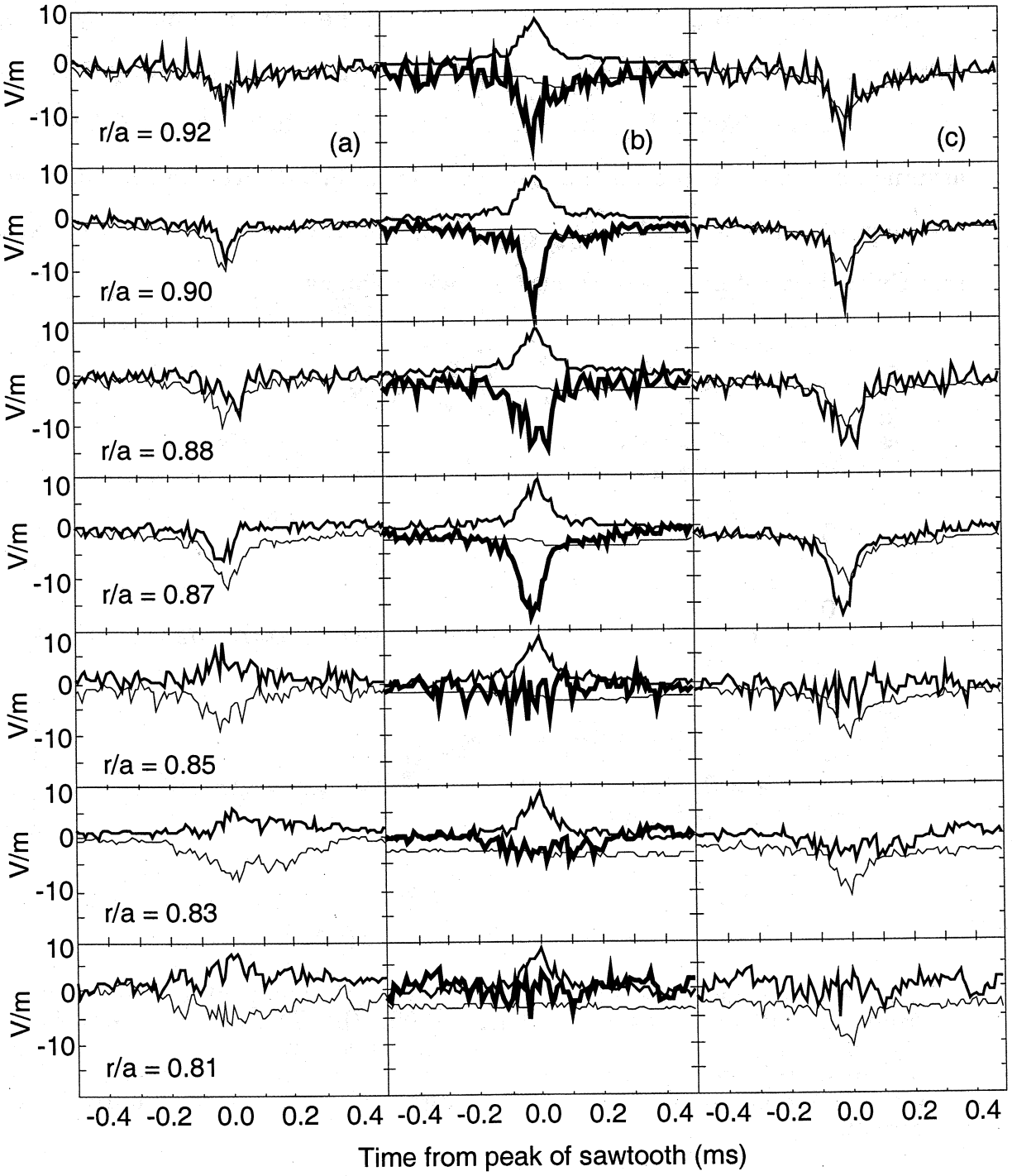

Figure 4.4. Edge Dynamo and Ohm's Law Profiles. Column (a) shows $\langle \tilde{v}_r \tilde{b}_t \rangle$ (thick line) and $\langle \tilde{v}_t \tilde{b}_r \rangle$ over a sawtooth vs. radius; note the change in sign of $\langle \tilde{v}_r \tilde{b}_t \rangle$ from r/a = 0.87 to r/a = 0.85. Column (b) shows the total dynamo $\langle \tilde{\boldsymbol{v}} \times \tilde{\boldsymbol{b}} \rangle_{\|}$, (thickest line), $\eta j_{\|}$ (thinnest line; negative), and $E_{\|}$ (medium line; positive). Column (c) shows the dynamo again (thick line) along with $\eta j_{\|} - E_{\|}$, showing the balance of Ohm's law.

insertable magnetic probe (or the magnetic coils in the Rogowski probe), simultaneous measurements of these four fluctuating quantities have been made and sawtooth-ensembled at multiple radii. The IDSP was mounted on one of MST's 4.5" ports at 19°P, while the magnetic probe was at the same toroidal location and 37°P and were inserted to the same depth as the IDSP to sample nearby on approximately the same flux surface. The results are shown in the first column of Figure 4.4. Here positive indicates the direction of increasing poloidal angle, i.e. the direction opposite the current. It can be seen that both terms are small but nonzero away from the peak of the dynamo event and rise to several V/m at the peak. Outside the reversal surface both terms are in the direction of the parallel current and contribute to the dynamo. At deeper radii the $\tilde{v}_r\tilde{b}_t$ term changes direction and competes with the $\tilde{v}_t\tilde{b}_r$ term, nearly cancelling the net dynamo effect.

At large radii the measured dynamo product balances Ohm's law extremely well (Figure 4.4(c)). As discussed in Chapter 1, this measurement is qualitatively consistent with earlier dynamo measurements using Langmuir probes. The electric field $E_{||}$ is negligible during the quiescent phase, while $\langle\tilde{\boldsymbol{v}}\times\tilde{\boldsymbol{b}}\rangle_{||}$ approximately accounts for $\eta j_{||}$ and both are small. As the velocity and magnetic fluctuations increase during the rising phase, both $\langle\tilde{\boldsymbol{v}}\times\tilde{\boldsymbol{b}}\rangle_{||}$ and $E_{||}$ rise to about 10 V/m; the two terms cancel while $\eta j_{||}$ remains small. In the decay phase the current magnitude rises modestly and compensates for a slight decrease in the magnitude of the fluctuation term to continue to balance $E_{||}$. Finally all three terms return to their low, pre-dynamo-event level.

The r/a = 0.92 plot of Figure 4.4(c) reveals two interesting characteristics of the dynamics of parallel Ohm's law. The first is the significant contribution of

the fluctuation-induced dynamo in balancing the process. Indeed, the contribution of the parallel current term in Ohm's law is surprisingly small during the rising phase of the dynamo event, while the dynamo balances a large induced $E_{||}$. The second observation is the remarkable agreement in time-dependence between the two plots, particularly during the decay phase of the dynamo event cycle, when $\eta j_{||}$ becomes more significant. Comparing $\langle \tilde{v} \times \tilde{b} \rangle_{||}$ with $-E_{||}$ alone does not yield nearly such good agreement during this part of the cycle. The assumption that η does not change much during the dynamo event cycle is validated by this observation.

At r/a of 0.87 to 0.90 the agreement of $\langle \tilde{v} \times \tilde{b} \rangle_{||}$ with $\eta j_{||} - E_{||}$ continues to be good, although slight discrepancies begin to appear just at the peak of the dynamo event, possibly indicating a slight increase of plasma resistivity or a contribution from other effects. However, at r/a $\leq$ 0.85 (deeper than the reversal surface), the dynamo term virtually disappears. This is true despite the fact that the magnitudes of $\tilde{v}_r$, $\tilde{v}_t$, $\tilde{b}_r$, and $\tilde{b}_t$ individually remain large.

4.5 Pseudo-spectral Analysis of Velocity and Magnetic Field

The B_p-pseudo-spectrum described in Chapter 2 has been computed for the local velocity and magnetic fluctuations at various radii (Figures 4.5 – 4.8). Here the n^{th} component of the pseudo-spectrum of the signal $\tilde{x}$ is

$$\tilde{x}_n = \frac{\left\langle \tilde{x}\tilde{B}_n \right\rangle}{\left|\tilde{B}_n\right| \cos\delta_n} = \tilde{x}\gamma_n ,$$

where $\tilde{B}_n$ is the magnetic mode of toroidal number n as resolved by the edge magnetic array, and γ_n and $\cos\delta_n$ are the correlation and phase of $\tilde{x}$ with this

mode. The results for the magnetic signals show the expected contribution from the n=6, 7, and 8 core-resonant tearing modes, peaking strongly at the sawtooth crash. The velocity fluctuations, on the other hand, show surprisingly small contributions from these modes. In fact, at most radii the correlation between velocity fluctuations and these modes drops at the crash. The n=1 and 2 modes show good correlation; given the safety factor profile (both modeled and, in the edge, measured) in MST, resonant modes with these toroidal numbers are known to correspond to m=0 modes resonant at the reversal surface.

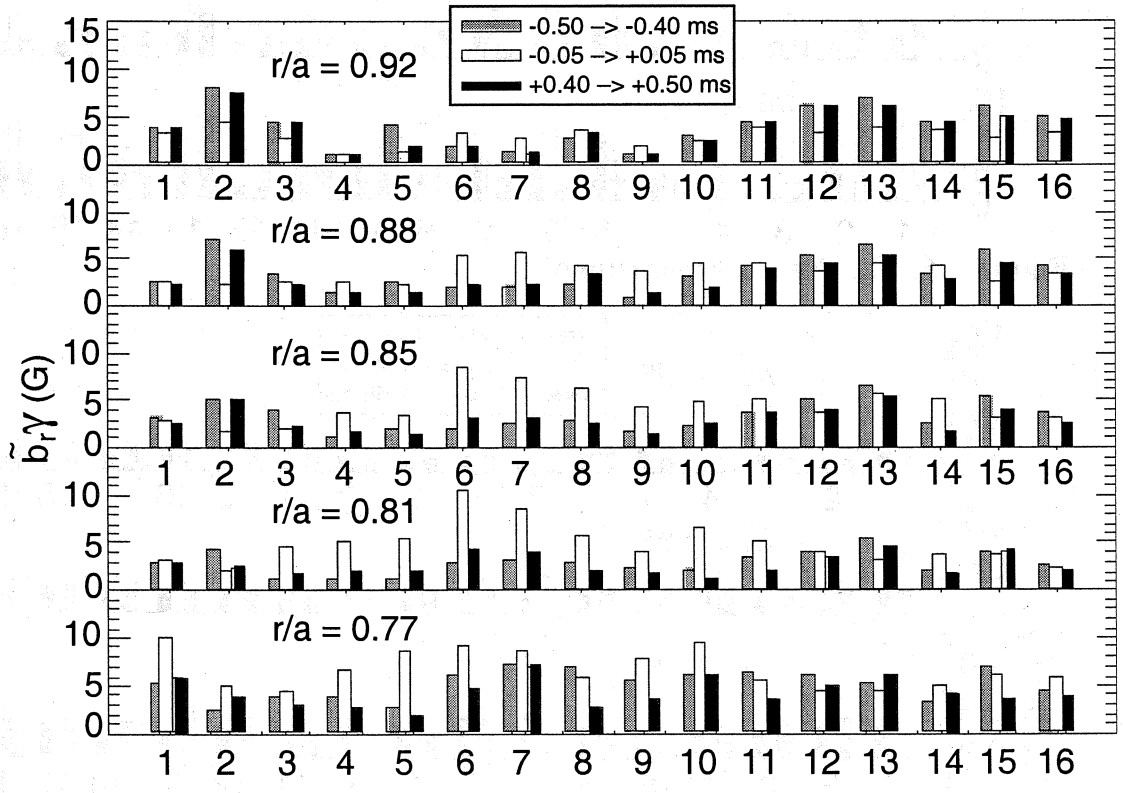

Figure 4.5. B_p-Pseudo-Spectrum of $\tilde{b}_r$. Shown are sawtooth ensemble results, averaged 0.45 ms before the crash (gray bars), at the crash (white bars), and 0.45 ms after the crash (black bars).

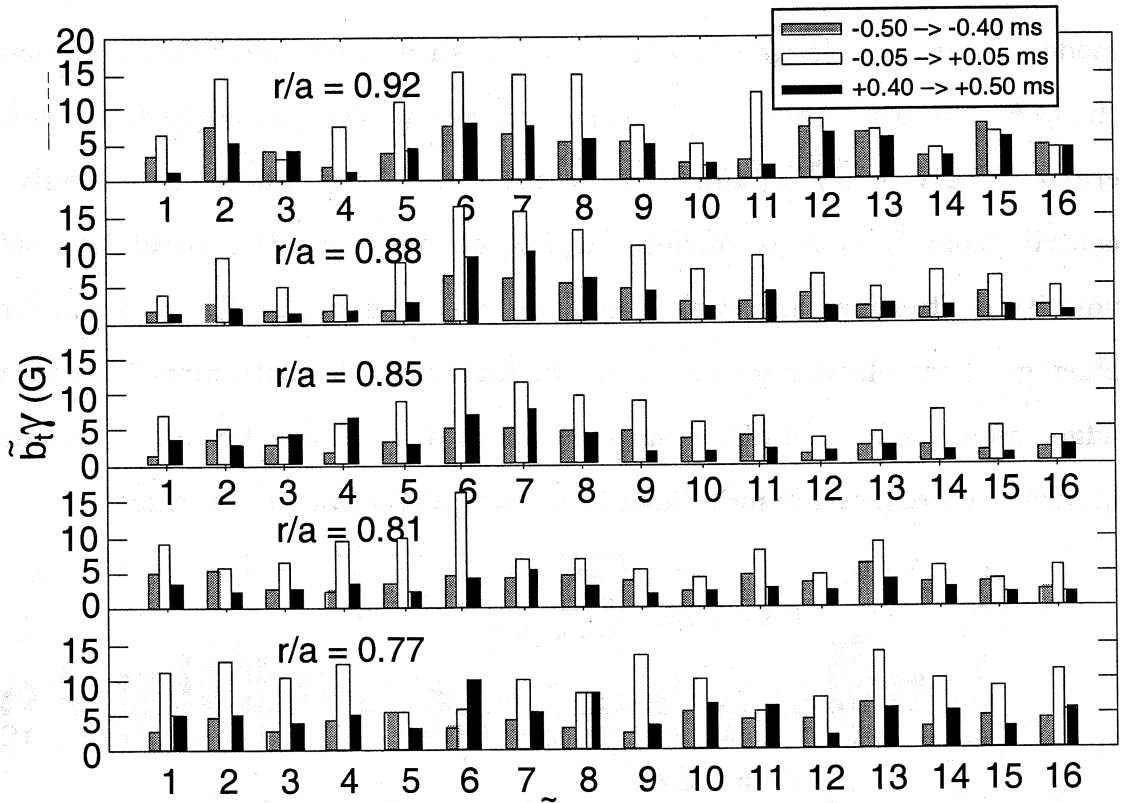

Figure 4.6. B_p-Pseudo-Spectrum of $\tilde{b}_t$.

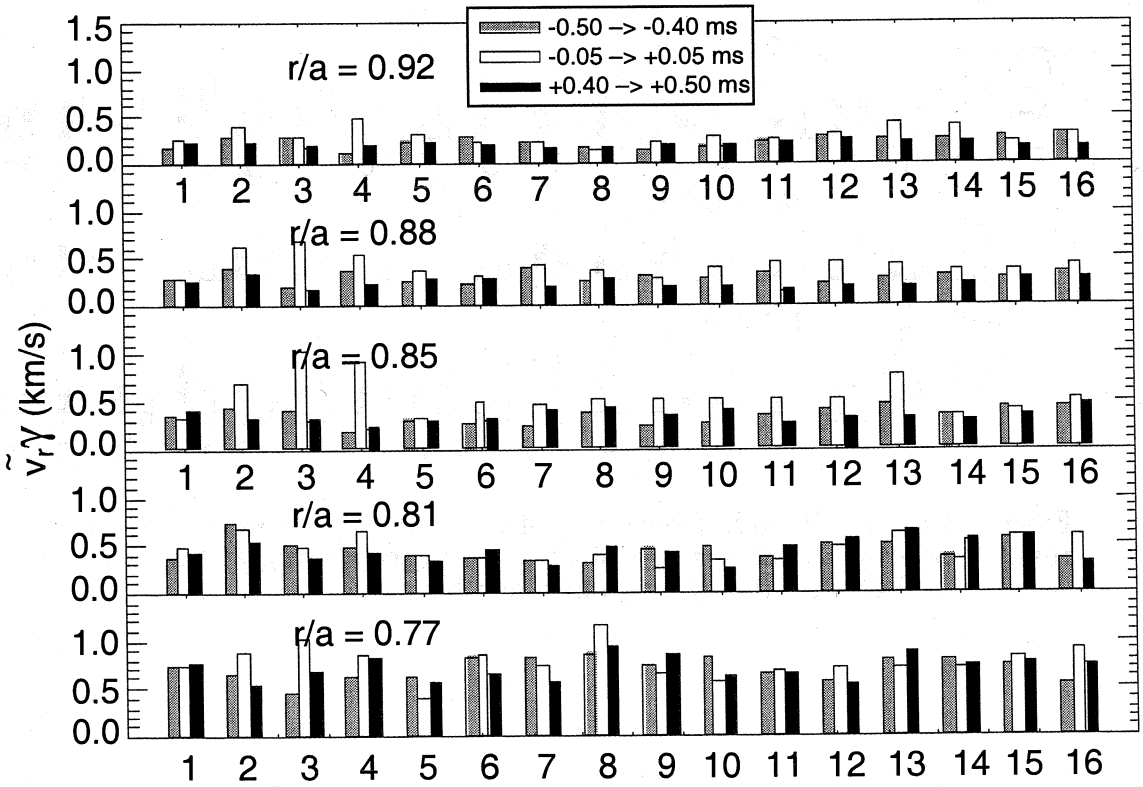

Figure 4.7. B_p-Pseudo-Spectrum of $\tilde{v}_r$.

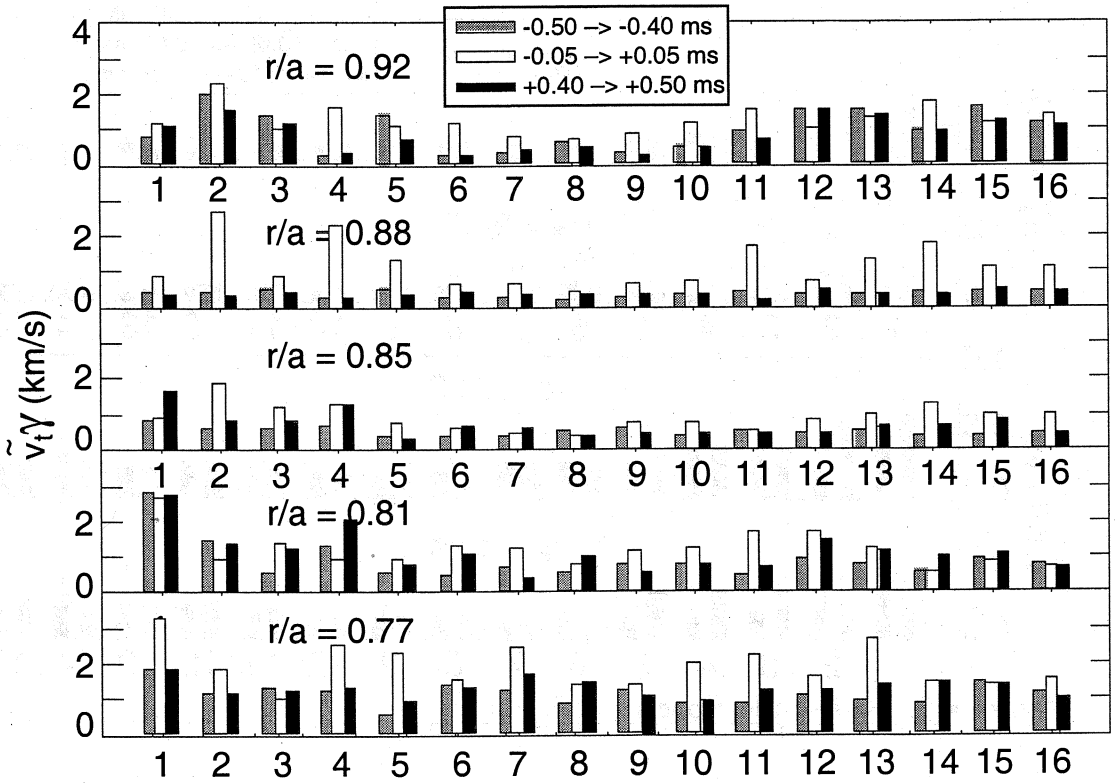

Figure 4.8. B_p-Pseudo-Spectrum of $\tilde{v}_t$.

Because calibration issues render the low-n results of the B_p array somewhat suspect, the analysis has been repeated for the velocity signals using the B_t coil set. From these spectra (Figure 4.9) it becomes clear that the correlated velocity fluctuations are dominated by low n, particularly n=1.

The m=0 modes in MST are subject to locking in the laboratory frame, especially during dynamo events. Thus a sawtooth ensemble of m=0 fluctuations runs the risk of sampling the phase of these m=0 modes nonuniformly, resulting in an ensemble which is not truly representative of a flux-surface average. Evidence of imperfect flux-surface sampling is given by the ensemble average of the amplitude (or the sine and cosine amplitudes individually) of a magnetic mode, which should be approximately zero in an appropriately phase-

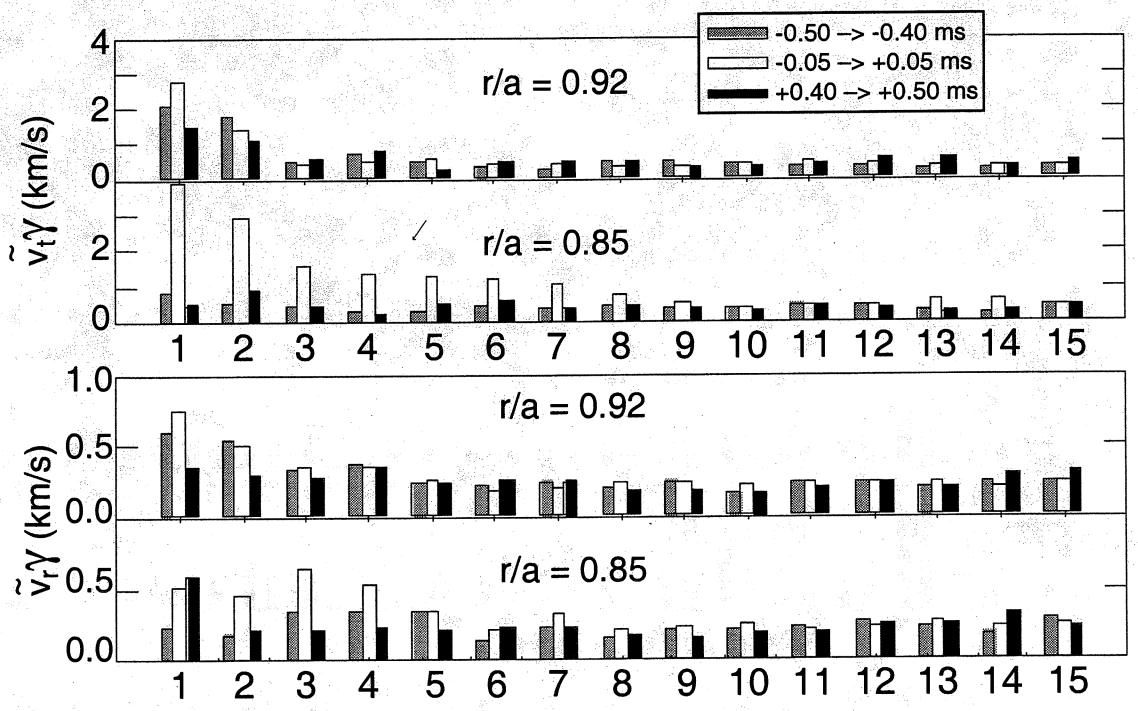

Figure 4.9. B_t-Pseudo-Spectra of $\tilde{v}_t$ and $\tilde{v}_r$.

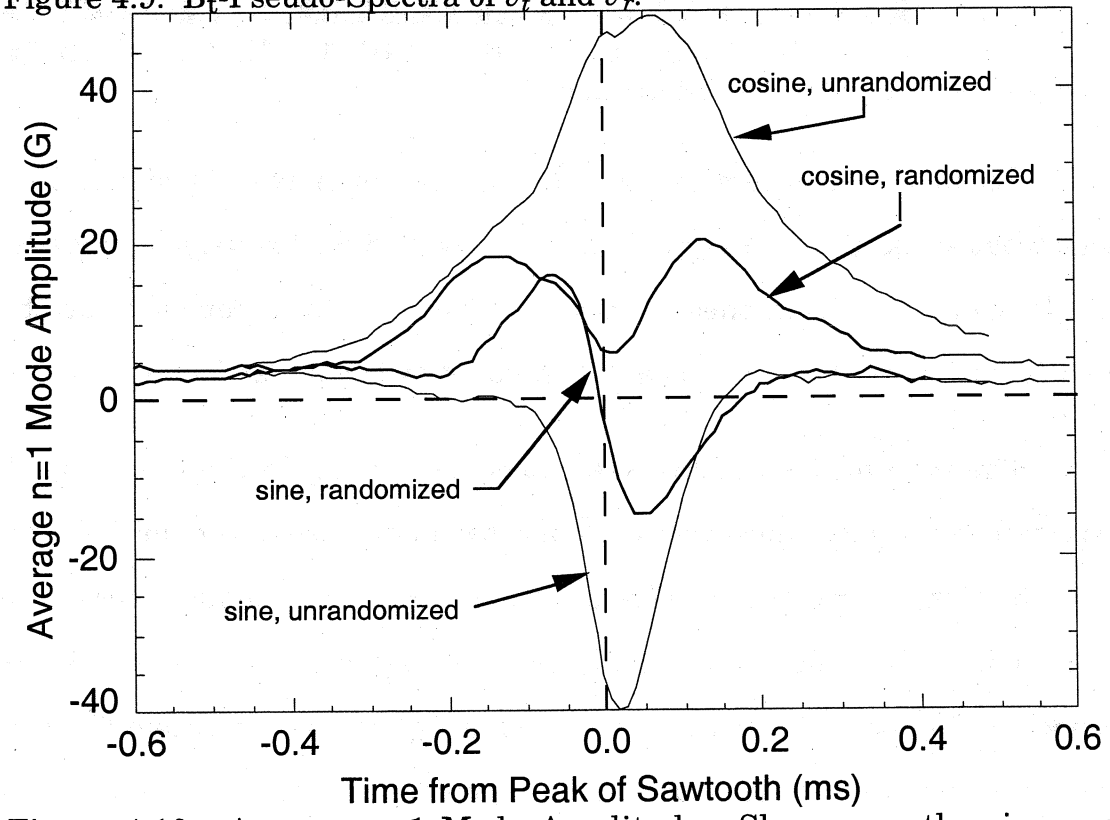

Figure 4.10. Average n=1 Mode Amplitude. Shown are the sine and cosine components of the n=1 mode from the B_t coils of the toroidal array over a sawtooth, for a phase-unrandomized (light line; larger) and a phase-randomized (heavy line; smaller) ensemble.

randomized ensemble. Both the average amplitude of n=1 mode sine and cosine components (Figure 4.10.) and a scatter plot of the ensembled sawteeth versus phase and amplitude of the n=1 mode (Figure 4.11.) indicate non-phase-randomized ensembles. To assess the effect of this nonuniform sampling on the velocity fluctuation correlations, the ensemble was thinned, leaving a collection of sawteeth uniformly distributed in n=1 phase and amplitude and giving a value close to zero for the average n=1 amplitude over the ensemble at time t=0 ms relative to the crash (Figure 4.11(b)). The correlation of the velocity fluctuations with the n=1 mode in this reduced ensemble is essentially unchanged from the larger ensemble, as seen in Figure 4.12, indicating that the nonuniform sampling is not a problem in this instance and allowing us to conclude that the correlated velocity spectrum is indeed dominated by the n=1 mode.

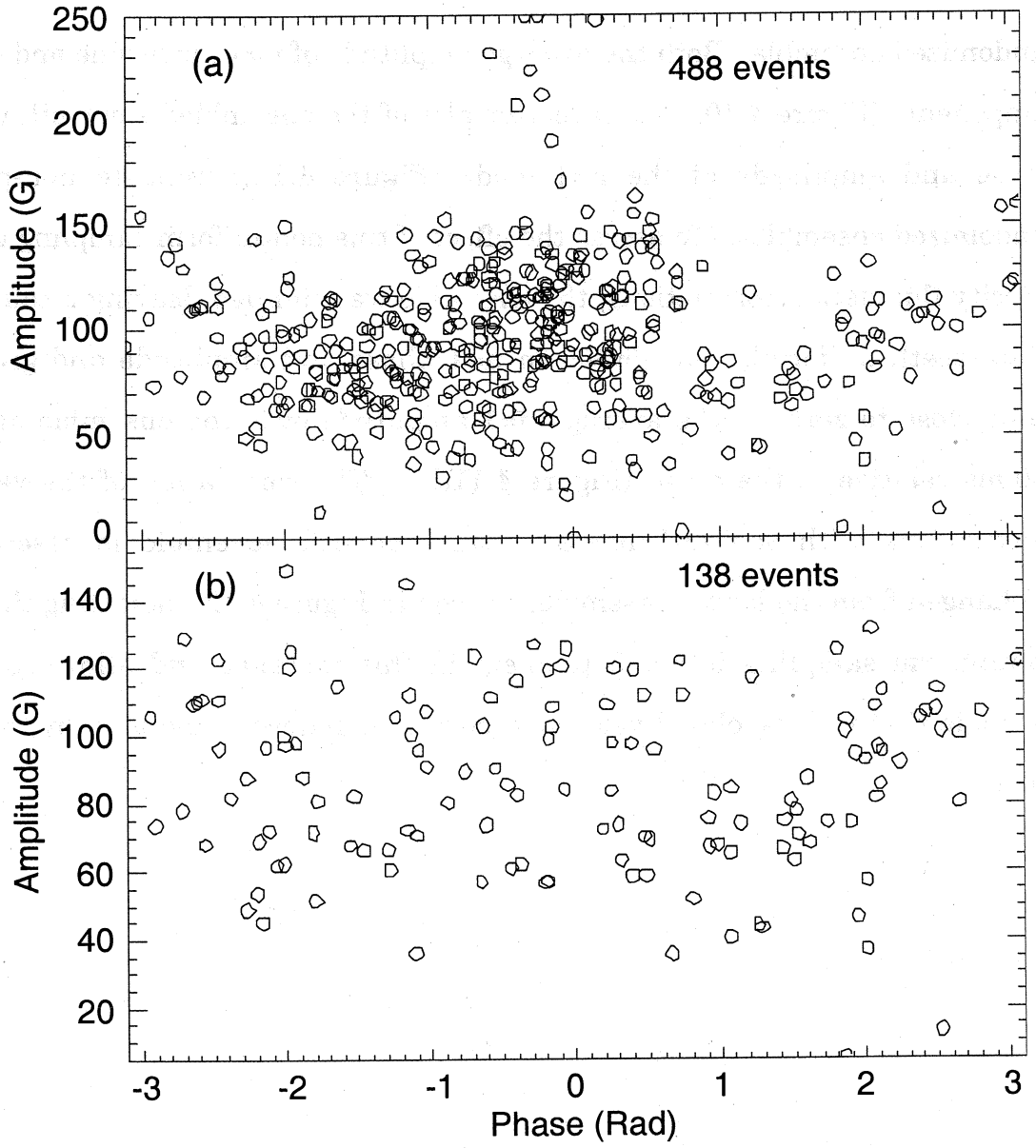

Figure 4.11. Phase and Amplitude of the n=1 Mode. (a) The unfiltered ensemble, showing uneven distribution in phase and amplitude. (b) The reduced ensemble.

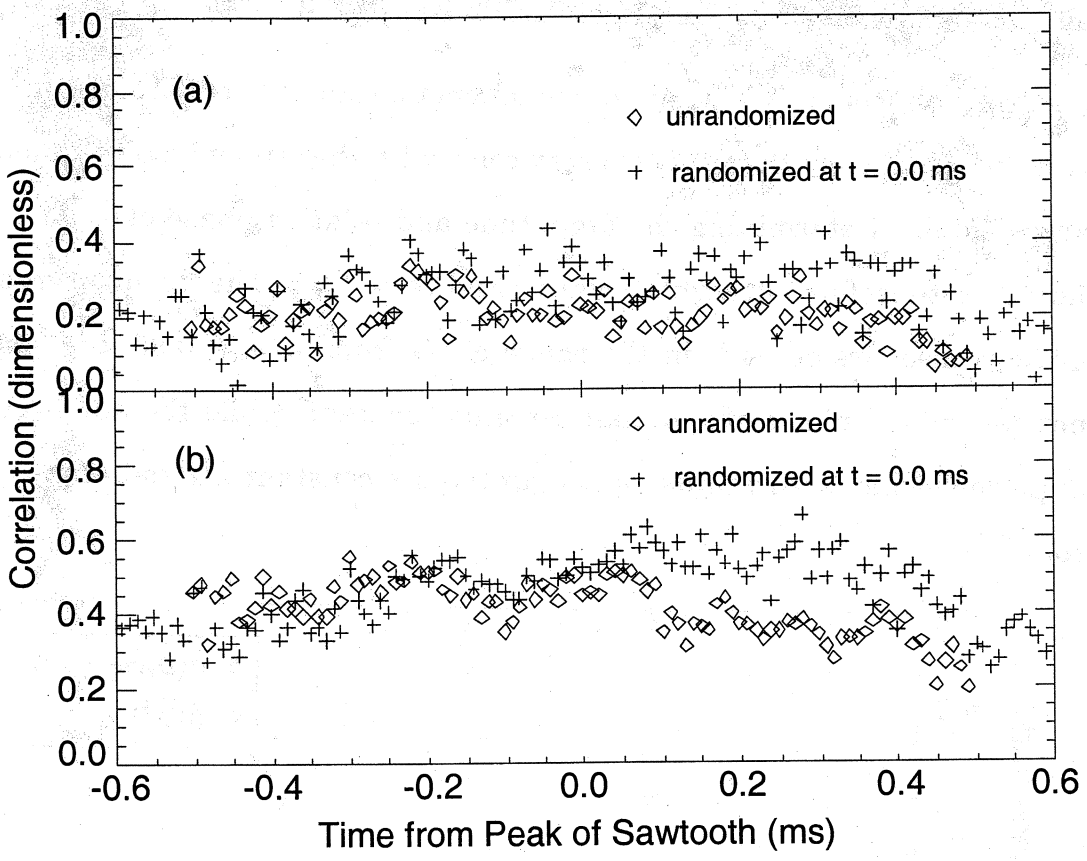

Figure 4.12. Correlations With and Without Randomization. Correlation of (a) $\tilde{v}_r$ and (b) $\tilde{v}_t$ with the n=1 cosine component. Correlations are essentially unchanged by randomization.

This result is significant. Although the local magnetic spectra include large amounts of power from the core-resonant tearing modes, these modes do not contribute to the local velocity spectra. The implication is that the tearing modes contribute to the velocity fluctuations only in the vicinity of their resonant surfaces, suggesting that the velocity eigenfunctions are localized to these regions and may mean that the immediate presence of magnetic islands plays a role in generating velocity fluctuations. This result is similar to what has been seen in the core of MST,[3] where the velocity fluctuations were seen to correlate with the core-resonant modes only near their rational surfaces.

4.6 Phase Profile of Velocity and Magnetic Field

As one would expect, the probe magnetic signals correlate extremely well with the signal from the toroidal array coils, with the strongest correlation at the largest radii. Determining the amplitude and relative phase of $\tilde{b}_r$ and $\tilde{b}_t$ with radius is therefore straightforward (Figure 4.13). The result agrees with previous measurements:[4] in the range of r/a from 0.75 to 0.95, the amplitude (not shown)and phase of $\tilde{b}_t$ remain roughly constant, while the amplitude of $\tilde{b}_r$ drops somewhat with radius as it maintains a constant $\pi/2$ radian phase shift from $\tilde{b}_t$.

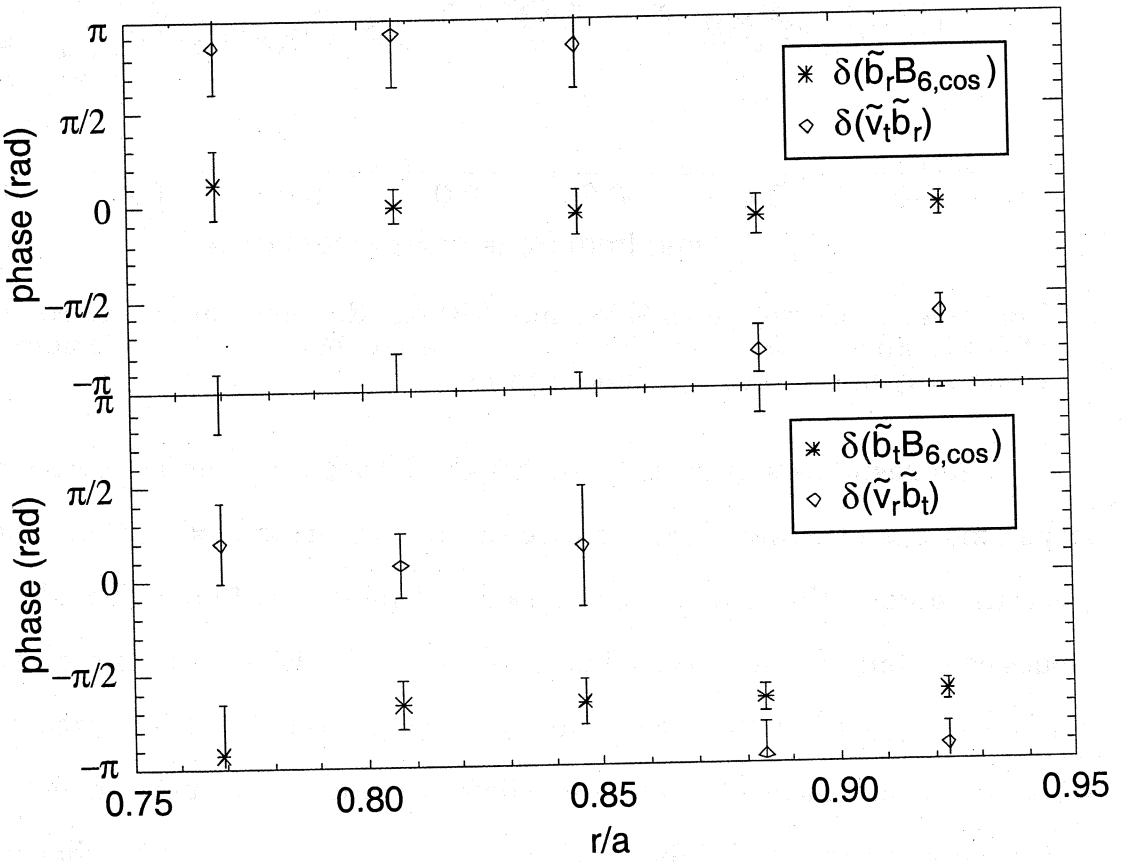

Figure 4.13. Phase Profiles of Magnetic Signals and Dynamo. Top: the phase of $\tilde{b}_r$ as referred to the cosine component of the n=6 mode (asterisks) and the relative phase of $\tilde{b}_r$ and $\tilde{v}_t$ (diamonds) vs. radius. Bottom: the phase of $\tilde{b}_t$ (asterisks) and relative phase of $\tilde{b}_t$ and $\tilde{v}_r$ (diamonds).

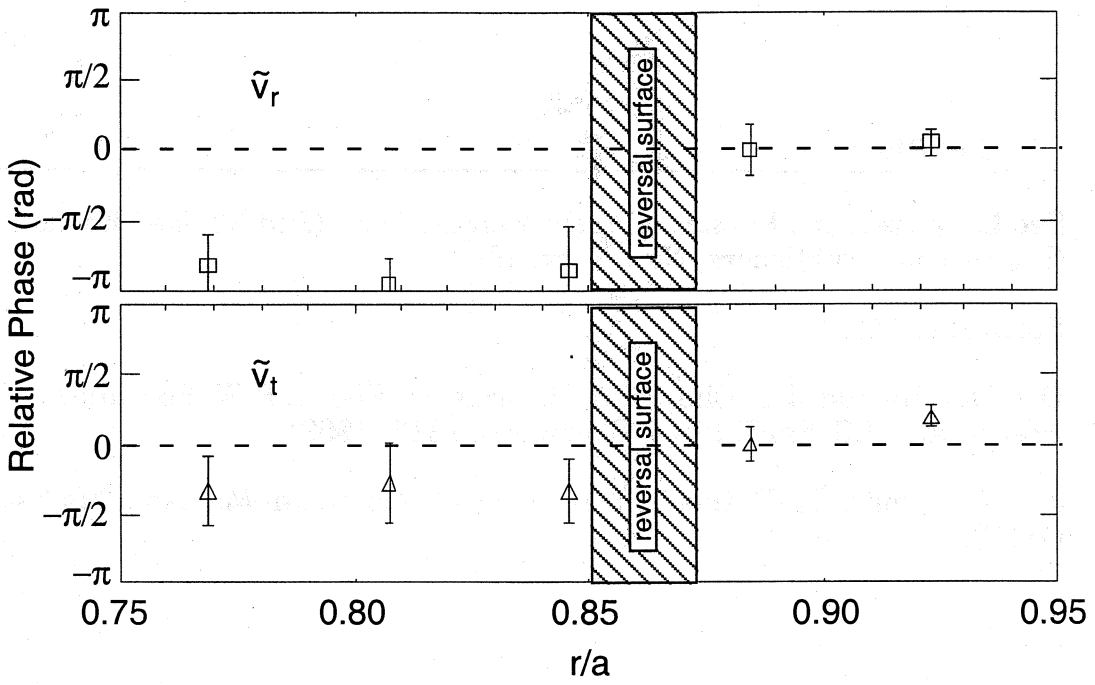

Figure 4.14. Relative Phase of$\tilde{v}_r$ and $\tilde{v}_t$. The radial velocity fluctuations (top) flip phase in the vicinity of the reversal surface. The change in the toroidal fluctuations is much smaller.

Because the correlations of the velocity fluctuations with edge magnetic signals is low and only significant at low frequencies, the phase of $\tilde{\boldsymbol{v}}$ is difficult to measure by direct comparison with these signals. However, armed with phase profiles of the magnetic fluctuations, the phases of $\tilde{v}_r$ and $\tilde{v}_t$ can be inferred from the dynamo correlations, $\langle \tilde{v}_r \tilde{b}_t \rangle$ and $\langle \tilde{v}_t \tilde{b}_r \rangle$. In particular, the sign change in $\langle \tilde{v}_r \tilde{b}_t \rangle$ with radius can be traced to a shift of π radians in the phase of $\tilde{v}_r$ relative to $\tilde{b}_t$. Since$\tilde{b}_t$ is constant in phase over this region, we conclude that the radial velocity fluctuation undergoes a phase flip of π radians across the reversal surface. The toroidal velocity fluctuations, meanwhile, nearly maintain their phase throughout this region, as indicated by a similar analysis of $\langle \tilde{v}_t \tilde{b}_r \rangle$ (Figures 4.13 and 4.14). To our knowledge, this constitutes the first measurement of the tearing mode parity of velocity fluctuations across a resonant surface.

REFERENCES

1 See L. Spitzer, Jr., *Physics of Fully Ionized Gases* (2nd Revised Edition) (Interscience Publishers, New York, 1962).

2 Spitzer, p. 143.

3 D.J. Den Hartog, J.T. Chapman, D. Craig, G. Fiksel, P.W. Fontana, S. C. Prager, and J.S. Sarff, Phys. Plasmas **6**, 1813 (1999).

4 J. T. Chapman. Ph.D. thesis, University of Wisconsin–Madison, Madison (1998).

5: *Review and Future Work*

5.1 Summary

Chapter 1 opens this dissertation by summarizing theoretical and experimental arguments for the presence of a fluctuation-induced dynamo in the RFP. These include applications of Cowlings theorem which demonstrate that the RFP magnetic field topology cannot maintain itself in steady state without the dynamo, modeling of the electric field and current in real RFP plasmas which show a discrepancy between the two, and nonlinear MHD computations which indicate the presence of correlated magnetic and velocity tearing fluctuations which produce an e.m.f. Section 1.2 reviews the previous dynamo measurements in the RFP, particularly core spectroscopic measurements in MST and extreme edge Langmuir probe measurements of $\tilde{\mathbf{E}} \times \mathbf{B}$ and $\nabla \tilde{\mathbf{P}} \times \mathbf{B}$ velocities in several RFP's. In Section 1.3 the distinctions of this work are highlighted, including their spatial localization, region of observation, and direct measurement of the total $\tilde{v}$. The results characterizing the edge velocity fluctuations as locally-resonant are previewed as well, as is the observation of the flip of phase of the radial fluctuations across the resonant surface. Section

1.4 anticipates the work's secondary results, observations of the equilibrium edge flows in the RFP.

Chapter 2 of this thesis begins with technical descriptions of the various diagnostic instruments used in the current investigations. They include the Ion Dynamics Spectrometer (IDS) and the optical probe (IDSP) along with a review of Doppler spectroscopic analysis and its particularities as applied to the IDSP, the insertable magnetic probe used for local magnetic fluctuation measurements, the insertable Rogowski probe used both for current measurements and redundant magnetic measurements, and the triple Langmuir probe with a description of how to infer local electron density from its signals. There follows a description of correlation ensemble techniques which includes mathematical definitions of statistical quantities referred to throughout the thesis. Finally, the chapter explains the application of these techniques in inferring a mode spectrum for a single-point measurement by comparison with edge magnetic diagnostics.

Chapter 3 investigates the details of the equilibrium flow profiles in the edge of MST. Section 3.1 provides a detailed sawtooth-ensembled profile of the toroidal flow velocity v_t in the region $0.75 < r/a < 0.95$. It shows linearly decreasing magnitude with radius and strong deceleration and re-acceleration during the dynamo event. The velocity throughout most of the region is in the direction of the plasma current, consistent with an $\mathbf{E} \times \mathbf{B}$ flow produced by a radially-outward $\mathbf{E}$, and it reverses direction upon reversal of the equilibrium poloidal magnetic field. Investigation of the time dependence of the plasma deceleration at a sawtooth versus radius reveals that the effect begins toward the core and propagates outward. If, as theory predicts, the deceleration is due

to torque on magnetic islands, then this measurement is consistent with growth of the core mode islands to a size with significant torque first, followed by growth of the edge magnetic islands.

Section 3.2 examines the poloidal flow profile over a sawtooth and finds that it is much less strongly affected by sawteeth. Flow is in the outboard-up direction regardless of the polarity of B_p, and decreases in magnitude toward the extreme edge. The parallel flow shows a stronger shear in the vicinity of the reversal surface than away from it. These measurements are combined with Langmuir probe equilibrium density measurements to determine the parallel momentum profile, which is seen to flatten during a sawtooth crash, consistent with momentum transport theory and previous core measurements.

Section 3.3 describes the spectrometer calibration necessary to make absolute radial flow velocity measurements. Evidence for an equilibrium inward v_r is given, including observed changes in radial velocity by as much as 10 km/s over a discharge and by a few km/s during a sawtooth.

Section 3.4 describes flow measurements during discharges with enhanced confinement due to biasing and current injection. The indication is that although the toroidal flow changes direction during biasing, the shear in the region $0.83 < r/a < 0.94$ does not change significantly.

Section 3.5 shows changes in the toroidal flow at a single radius in discharges with an applied external poloidal current drive (PPCD). The flow changes character both at the start of PPCD and again with the onset enhanced PPCD confinement ("SDE-free") periods.

The chapter concludes (Section 3.6) with a measurement of the pitch angle of the magnetic field in the edge, significant mainly as it indicates the position of the reversal surface as a function of time relative to the dynamo event.

The main results of this work, namely the measurements of the edge dynamo fluctuations, are presented in Chapter 4. The first section of this chapter presents a derivation from the two-fluid equations of motion of the form of Ohm's law under study. Sections 4.2 and 4.3 describe the results of the parallel induced e.m.f. and parallel current, respectively. The electric field is found to approximate zero away from a dynamo event and to become large during the event, while the current is small but nonzero in the quiescent period and rises slowly and modestly during the sawtooth. Section 4.4 shows the dynamo e.m.f., which balances Ohm's law very well at the extreme edge but is seen to vanish at the smallest radii measured This cancellation is found to be due to competition between the two components of the dynamo, namely $\langle \tilde{v}_r \tilde{b}_t \rangle$ and $\langle \tilde{v}_t \tilde{b}_r \rangle$.

Section 4.5 demonstrates from pseudo-spectral analysis that the dynamo-inducing velocity fluctuations are of poloidal mode number m=0, as inferred from the predominance of toroidal mode numbers n=1 and 2 in the spectrum. In Section 4.6 the dynamo velocity fluctuations are shown to have the proper tearing mode parity for fluctuations resonant at the reversal surface. We conclude that although the amplitude of the core tearing modes is significant in the edge, they do not contribute to the dynamo there; instead, the edge measurements combined with similar core measurements made previously indicate that only locally-resonant fluctuations produce dynamo, suggesting that magnetic reconnection is a necessary ingredient.

5.2 Future work

The present work raises some questions which would be worth pursuing through future experiments. Most importantly, although the dynamo has been observed in the edge and found to balance Ohm's law, in the "near edge" of $0.81 < r/a < 0.85$ the dynamo has been observed to be self-defeating, in the sense that the two contributions to $\langle \tilde{v} \times \tilde{b} \rangle_{||}$ cancel each other. The current drive in this region remains to be identified. One explanation is that the dynamo is in fact active in this region, but involves fluctuations of wave number too high to be resolved by the IDSP. Another is the presence in this region of other sources of e.m.f. from the generalized Ohm's law, such as the $\langle \tilde{j} \times \tilde{b} \rangle$ Hall effect, which we reasoned in Section 4.1 was small as long as the dynamo remains significant. Finally it may become necessary to abandon MHD in this region in favor of a "kinetic dynamo", a theory which explains current and flux generation through stochastic transport of electrons out from the core.[1]

It would be satisfying also to pin down the Ohm's law contribution from the current more precisely. The limitation at the moment is on measurements of Z_{eff} which prevent accurate estimates of the resistivity η. Although I am confident that true measurements of η will not exceed the reasonable limits on it used herein, a time-dependent measurement might help to account for slight discrepancies in Ohm's law observed at the peak of the sawtooth. These differences would, for example, be explained by a slight increase in Z_{eff} at the crash expected to accompany the transport of higher-Z impurities from the core at that time.

Another outstanding issue in these measurements is the large inward radial flow. Of first priority is to rule out a probe-induced anomaly. A

straightforward approach would be to construct a new IDSP with two differences from the current model: (1) the light-collecting holes should be raised out of the plane of the probe stock to rule out finite Larmor radius effects or other interference which may currently be caused by the backstop of the viewing area, and (2) the entire viewing plane should be rotated by 90°, allowing the radial velocity to be calculated from the difference in Doppler shift of the two views rather than the average and allowing absolute v_r measurements without absolute calibration of the spectrometer.

In addition to the equilibrium flow and dynamo studies that have been accomplished so far, an area of RFP physics which ought to lend itself to investigation with the IDSP is particle transport. With local density fluctuation measurements $\tilde{n}$ from Langmuir probes or even edge chords of MST's FIR interferometer, the total fluctuation-induced particle transport is given by $\langle \tilde{n}\tilde{v}_r \rangle$. Unfortunately, attempts so far to measure this with the IDSP have been unsuccessful, yielding no correlation between the velocity and density fluctuations. This contradicts past and currently-underway Langmuir probe measurements in MST[2] as well as equilibrium modeling. The immediate next steps will be to correlate IDSP $\tilde{v}_r$ with those from a Langmuir probe, and to determine the k-spectrum of the contributing fluctuations as seen by the Langmuir probe to see if they are too small to be resolved by the IDSP. If some form of the IDSP manages to measure these fluctuations, the relative contribution to particle transport from magnetic fluctuations can then be measured through various correlations of $\tilde{n}$, $\tilde{b}_r$, and $\tilde{v}_{\|}$.

Other possible experiments using IDSP technology require significant modifications to the spectrometry system. The first which should be undertaken

is to provide the IDSP with a spectrometer with finer wavelength resolution. This will provide edge ion temperature measurements for the first time on MST. Physics issues to be addressed by this upgrade include ion energy transport and, since multiple simultaneous temperature measurements would be available, anomalous ion heating and ion temperature anisotropy. Scientists at the Magnetic Reconnection Experiment (MRX) have in fact borrowed our IDSP recently and used it in conjunction with a high-resolution spectrometer to make temperature measurements with the same HeII line, demonstrating feasibility.[3]

The principle of insertable optical diagnostics pioneered by the IDSP opens the door to a host of diagnostics opportunities. Ideas which come to mind which would be worth feasibility study include an interferometry/polarimetry probe and a Thomson scattering probe. Even more intriguing, both because it involves measurement of an elusive plasma parameter which has never succumbed to direct observation and because technologically it involves the same kind of spectroscopy for which the IDSP has already been proven useful, is the Plasma Viscosity Probe. Although only germinal in conception, the theoretical basis for such a diagnostic is given below for future reference.

The task of measuring plasma viscosity involves measuring asymmetric, non-Maxwellian characteristics of the ion velocity distribution, and would at first blush therefore seem to require unrealistically high precision in measurement of small distortions in the three-dimensional distribution function. As it turns out, however, the exact shape of the distribution function does not need to be known in great detail in order to calculate the plasma pressure tensor; it is sufficient to know completely the second-order moment of the distribution.

In general, given a distribution f(x,y,z), the projection of this distribution onto an axis t at angle θ from x to y and an angle ϕ from the z axis to the x–y plane is

$$P(\theta,\phi,t) = \iiint f(x,y,z)\delta(x\cos\theta\sin\phi + y\sin\theta\sin\phi + z\cos\phi - t)dxdydz.$$

Note that if x, y, and z are interpreted as velocity-space coordinates and f is the ion velocity distribution, then this projection P is exactly what is measured by spectroscopy with a line of sight oriented in the (θ,ϕ) direction; in that case the variable t can be thought of as the component of velocity in the direction of the line of sight, or equivalently as wavelength in the case of Doppler spectroscopy. Physical quantities such as velocity, temperature, and viscosity are then calculated from moments of this distribution with respect to t. The l^{th} moment of the projection P, denoted $M_l(\theta,\phi)$, is given by

$$M_l(\theta,\phi) = \int P(\theta,\phi,t)\,t^l\,dt\,.$$

In particular, the 2^{nd} moment (related to temperature and viscosity) is given by

$$\begin{aligned} M_2(\theta,\phi) &= \int\int\int f(x,y,z)(x\cos\theta\sin\phi + y\sin\theta\sin\phi + z\cos\phi - t)^2 \\ &\equiv X^2\cos^2\theta\sin^2\phi + Y^2\sin^2\theta\sin^2\phi + Z^2\cos^2\phi \\ &\quad + 2XY\cos\theta\sin\theta\sin^2\phi + 2XZ\cos\theta\cos\phi\sin\phi + 2YZ\sin\theta\cos\phi\sin\phi, \end{aligned}$$

where $XY \equiv \iiint f(x,y,z)xydxdydz$ and similarly for XX, XZ, YZ, etc. Thus measurement of M_2 for six appropriate choices of (θ,ϕ) are thus necessary and sufficient to determine M_2 uniquely for all (θ,ϕ).

These six measurements of M_2 then give six linear equations in the six independent components of the pressure tensor which can be solved for by a

simple linear inversion. Then the total pressure tensor Π (including temperature and viscosity) is proportional to

$$\begin{pmatrix} X^2 & XY & XZ \\ XY & Y^2 & YZ \\ XZ & YZ & Z^2 \end{pmatrix}.$$

For the purposes of constructing a viscosity probe, straightforward choices for the orientations (θ,ϕ) of the six lines of sight are:

$(0,0)$, $(0,\pi/4)$, $(0,\pi/2)$,	(3 lines of sight in X–Z plane, determine X^2, XZ, Z^2)
$(\pi/4,0)$, $(\pi/2,0)$,	(2 lines of sight in X–Y plane, determine XY, Y^2)
and $(\pi/2,\pi/4)$	(line of sight in Y–Z plane, determines YZ).

With such a construction and enough spectrometers to make six spectrometry measurements at high enough wavelength resolution to compute second moments of the Doppler-broadened distributions, then, the plasma viscosity can be directly computed.

REFERENCES

1 A.R. Jacobson and R.W. Moses, Phys. Rev. A **29**, 3335 (1984).

2 T.D. Rempel *et al.*, Phys. Fluids B **4**, 2136 (1992); C.-S. Chiang, private communication.

3 S.C. Hsu *et al.*, Princeton Plasma Physics Laboratory, private communication.